

AD-A183 043

LARGE-SCALE PLASMA DENSITY FLUCTUATIONS MEASURED WITH
THE HILAT SATELLITE (U) REGIS COLL. RESEARCH CENTER
WESTON MA D R WEIMER 01 APR 87 SCIENTIFIC-2

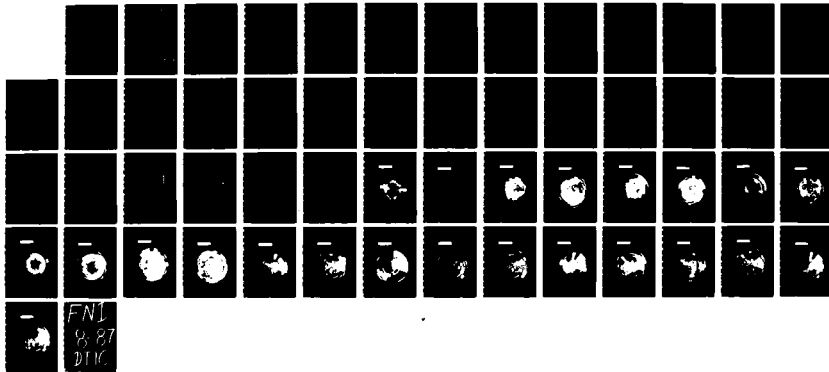
1/1

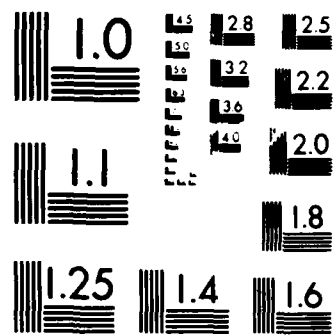
UNCLASSIFIED

AFGL-TR-87-0110 F19628-86-K-0045

F/G 4/1

NL





MICROCOPY RESOLUTION TEST CHART
NATIONAL BUREAU OF STANDARDS-1963-A

AD-A183 043

1.7
DTC_EILE COPY

AFGL-TR-87-0110

Large-Scale Plasma Density Fluctuations Measured with
the HILAT Satellite at 830 Km Altitude

D. R. Weimer

Regis College Research Center
235 Wellesley St.
Weston, MA 02193

1 April 1987

Scientific Report #2

APPROVED FOR PUBLIC RELEASE; DISTRIBUTION UNLIMITED

AIR FORCE GEOPHYSICS LABORATORY
AIR FORCE SYSTEMS COMMAND
UNITED STATES AIR FORCE
HANSOM AIR FORCE BASE, MASSACHUSETTS 01731

S AUG 07 1987 D

E

" This technical report has been reviewed and is approved for publication"



FREDERICK J. RICH
Contract Manager



NELSON C. MAYNARD
Branch Chief

FOR THE COMMANDER



RITA C. SAGALYN
Division Director

This report has been reviewed by the ESD Public Affairs Office (PA) and is releasable to the National Technical Information Service (NTIS).

Qualified requestors may obtain additional copies from the Defense Technical Information Center. All others should apply to the National Technical Information Service.

If your address has changed, or if you wish to be removed from the mailing list, or if the addressee is no longer employed by your organization, please notify AFGL/DAA, Hanscom AFB, MA 01731. This will assist us in maintaining a current mailing list.

Do not return copies of this report unless contractual obligations or notices on a specific document requires that it be returned.

REPORT DOCUMENTATION PAGE

1a REPORT SECURITY CLASSIFICATION Unclassified		1b. RESTRICTIVE MARKINGS	
2a SECURITY CLASSIFICATION AUTHORITY		3. DISTRIBUTION/AVAILABILITY OF REPORT Approved for public release; distribution unlimited.	
2b. DECLASSIFICATION/DOWNGRADING SCHEDULE		5. MONITORING ORGANIZATION REPORT NUMBER(S) AFGL-TR-87-0110	
4 PERFORMING ORGANIZATION REPORT NUMBER(S)	7a. NAME OF MONITORING ORGANIZATION Air Force Geophysics Laboratory		
6a. NAME OF PERFORMING ORGANIZATION Regis College Research Center	6b OFFICE SYMBOL (If applicable)	7b ADDRESS (City, State, and ZIP Code) Hanscom AFB, MA 01731	
6c. ADDRESS (City, State, and ZIP Code) 235 Wellesley St. Weston, MA 02193	8. PROCUREMENT INSTRUMENT IDENTIFICATION NUMBER F19628-86-K-0045		
8a. NAME OF FUNDING/SPONSORING ORGANIZATION	8b OFFICE SYMBOL (If applicable)	10. SOURCE OF FUNDING NUMBERS	
8c. ADDRESS (City, State, and ZIP Code)		PROGRAM ELEMENT NO. 61102F	PROJECT NO. 2311
11. TITLE (Include Security Classification) Large-scale plasma density fluctuations measured with the HILAT satellite at 830 km altitude (unclassified)		TASK NO. 2311G5	WORK UNIT ACCESSION NO. 2311G5AF
12 PERSONAL AUTHOR(S) Weimer, Daniel R.	14. DATE OF REPORT (Year, Month, Day) 1987 April 1		
13a. TYPE OF REPORT Scientific #2	13b TIME COVERED FROM 2DEC86 TO 30NOV89	15 PAGE COUNT 54	
16. SUPPLEMENTARY NOTATION			
17. COSATI CODES		18. SUBJECT TERMS (Continue on reverse if necessary and identify by block number) plasma irregularities, ionosphere, scintillations, HILAT	
FIELD	GROUP	SUB-GROUP	
19. ABSTRACT (Continue on reverse if necessary and identify by block number)			
<p>Measurements from the plasma monitor on the HILAT satellite have been used to map the distribution of large-scale fluctuations in the density of plasma at high latitudes. Digital filtering has been used to separate the original data into three frequency bands. The output from the middle band-pass filter has been used to count and map the distribution of large-scale plasma density enhancements. Maps of "blob" distribution are drawn as a function of magnetic local time and invariant latitude, for both low and high magnetic activity. To serve as a point of reference the same filtering and counting techniques are applied to measurements of the ion drift velocity to show the distribution of electric field fluctuations. Additionally, from the power levels measured at two different frequencies, the average spectral slopes of both the plasma density and electric field have been mapped.</p> <p>The results show that large-scale plasma enhancements are created in the auroral zone and are transported away from the production regions by convection. Movement of blobs from the cusp to polar cap is very prominent. The spectral slope of the plasma density (continued)</p>			
20. DISTRIBUTION-AVAILABILITY OF ABSTRACT <input checked="" type="checkbox"/> UNCLASSIFIED/UNLIMITED <input type="checkbox"/> SAME AS RPT <input type="checkbox"/> DTIC USERS		21. ABSTRACT SECURITY CLASSIFICATION Unclassified	
22a. NAME OF RESPONSIBLE INDIVIDUAL Frederick J. Rich		22b. TELEPHONE (Include Area Code) (617) 377-2431	22c. OFFICE SYMBOL AFGL/PHG

19. ABSTRACT (continuation)

is significantly increased in the night side, from 23 to 2 hour magnetic local time. The intermediate-scale plasma irregularities appear to be dissipated in this region. Enhanced radio scintillations had been measured with the HILAT radio beacon in the same locations.

TABLE OF CONTENTS

I. Introduction	1
II. Experimental Procedure	3
Frequency Filtering	3
Data Base	6
Irregularity Distribution Maps	7
Spectral Slopes	9
III. Discussion of Results	11
IV. Summary	14
V. Acknowledgments	16
VI. References	16
VII. Figure Captions	18

Accession For	
NTIS GRA&I	<input checked="" type="checkbox"/>
DTIC TAB	<input type="checkbox"/>
Unannounced	<input type="checkbox"/>
Justification _____	
By _____	
Distribution/ _____	
Availability Codes _____	
Dist	Avail and/or Special
A-1	



I. Introduction

Irregularities in the Earth's high-latitude ionospheric plasma occur on scales ranging from hundreds of kilometers down to centimeters. Plasma instability processes are assumed to be responsible for the structuring of the plasma density at intermediate (kilometer) and small (meter) scales. These small-scale variations are of concern since they can cause radio wave scintillation and disrupt communications with satellites. At large scales (tens to hundreds of kilometers) the variations are governed by plasma production, transport, and decay processes. Interactions between the solar wind, magnetosphere, and ionosphere are responsible for the production and transport of the large-scale plasma irregularities. Instabilities which feed on large-scale plasma gradients couple the different scale-length regimes.

A review of the theoretical and experimental work done with the subject of ionospheric irregularities has been written by Fejer and Kelley [1980]. In order to further understand the high-latitude plasma structure on a global basis it is necessary to determine how, when, and where the irregularities are produced, how long they last, and how they are transported by plasma convection [Vickrey, 1982]. Kelley et al. [1982] have done a theoretical study in which production, decay, and convection models are combined to produce a map of the amplitudes of kilometer-scale electron density irregularities. A very recent paper by Weber et al. [1986] has shown that large-scale patches convecting across the polar cap can produce small-scale structure.

The intent of this report is to present the results of measurements of

plasma irregularities obtained with the HILAT satellite. HILAT was launched on June 27, 1983 with a complement of five experiments, with the intent to probe irregularities in the ionospheric plasma which produce radio wave scintillation [Fremouw and Wittwer, 1984; Potocki, 1984]. The five instruments are a coherent radio beacon, plasma monitor, vector magnetometer, electron spectrometer, and auroral ionospheric mapper. The satellite orbit is nearly circular at an altitude of 820 km and 82° inclination. Data are collected by means of real-time transmissions to high-latitude ground stations. The three primary stations are located at Tromso, Norway; Sondre Stromfjord, Greenland; and Churchill, Manitoba.

The data in this report has been obtained from the plasma monitor on HILAT. This instrument can measure plasma density and drift velocity (electric fields) using a Retarding Potential Analyzer (RPA) and an Ion Drift Meter (IDM). The RPA measures ion densities at a frequency of 1.5 Hz, or one sample every 2/3 second. Descriptions of the plasma instrument's design, operation, and data processing procedures can be found in the reports by Rich and Heelis [1983], Rich et al. [1984], and Basinska [1984].

As the HILAT orbital velocity is 7.44 km-sec^{-1} , the plasma density sampling rate corresponds to a spatial sampling interval of about 5 km. Due to this instrumental constraint the small-scale structures cannot be measured. Therefore, the experimental investigation described here has been focused on the large-scale plasma density enhancements, which may be the source for the smaller-scale structures. The distribution of the large-scale plasma "patches" has been measured, which indicates where the irregularities originate and how they move. Additionally, the power at two different scales has been measured in order to estimate spectral slopes.

This shows the relationship between the patches of different sizes.

II. Experimental Procedure

Frequency Filtering

Examination of graphs of plasma density as a function of time, as measured with the RPA, shows that the plasma at 830 km altitude has a great deal of structure. The data has different characteristics at different scales. On the largest scale there are gradients which result from the differences in ionization between the dayside and nightside. Particle precipitation within the auroral zone also produces large-scale gradients. A different class of structure appears within the auroral zone on the same scale as discrete auroral arcs, a few tens of kilometers across. Some of these ionization enhancements which are produced in the aurora, however, appear to be able to move outside of the production region due to convection.

The plasma drift velocity (electric field) also has scale-length dependent features. On the largest scale there is the convection electric field, and there are also smaller-scale variations within the auroral zone. The arc-sized plasma density and electric field variations are often co-located within the same general areas but there does not appear to be a consistent phase correlation between the two.

The first step in the analysis of the data was to use digital filtering to separate the variations which occur at different scale sizes. In other words, the measured signals were passed through three filters (low-pass, band-pass, and high-pass) to separate the different frequency components. The filtering was accomplished by a Fourier transform of the data, followed by a multiplication by a window function in the frequency domain and an

inverse Fourier transform back to the time domain. Window functions with Hanning-type roll-offs were used for the filtering since rectangular windows, which have sharp cut-offs, result in distortion and "ringing" in the filtered signals. For the low-pass filter the amplitude response is :

$$A_1(f) = \frac{1}{2} \left\{ 1 + \cos \frac{\pi f}{2f_1} \right\} \quad 0 \leq f \leq 2f_1 \quad (1a)$$

$$A_1(f) = 0 \quad 2f_1 \leq f \leq f_N \quad (1b)$$

where f_1 is the "cut-off" frequency where the amplitude response is 1/2 and f_N is the Nyquist frequency (one-half the sample frequency). The high-pass filter amplitude response is:

$$A_3(f) = 0 \quad 0 \leq f \leq f_2 \quad (2a)$$

$$A_3(f) = \frac{1}{2} \left\{ 1 - \cos \frac{\pi(f-f_2)}{2(f_3-f_2)} \right\} \quad f_2 \leq f \leq (2f_3 - f_2) \quad (2b)$$

$$A_3(f) = 1 \quad (2f_3 - f_2) \leq f \leq f_N \quad (2c)$$

where f_3 is the high-pass cut-off frequency. The medium-frequency band-pass filter is the complement of the other two filters:

$$A_2(f) = \frac{1}{2} \left\{ 1 - \cos \frac{\pi f}{2f_1} \right\} \quad 0 \leq f \leq 2f_1 \quad (3a)$$

$$A_2(f) = 1 \quad 2f_1 \leq f \leq f_2 \quad (3b)$$

$$A_2(f) = \frac{1}{2} \left\{ 1 + \cos \frac{\pi(f-f_2)}{2(f_3-f_2)} \right\} \quad f_2 \leq f \leq (2f_3 - f_2) \quad (3c)$$

$$A_2(f) = 0 \quad (2f_3 - f_2) \leq f \leq f_N \quad (3d)$$

inverse Fourier transform back to the time domain. Window functions with Hanning-type roll-offs were used for the filtering since rectangular windows, which have sharp cut-offs, result in distortion and "ringing" in the filtered signals. For the low-pass filter the amplitude response is :

$$A_1(f) = \frac{1}{2} \left\{ 1 + \cos \frac{\pi f}{2f_1} \right\} \quad 0 \leq f \leq 2f_1 \quad (1a)$$

$$A_1(f) = 0 \quad 2f_1 \leq f \leq f_N \quad (1b)$$

where f_1 is the "cut-off" frequency where the amplitude response is 1/2 and f_N is the Nyquist frequency (one-half the sample frequency). The high-pass filter amplitude response is:

$$A_3(f) = 0 \quad 0 \leq f \leq f_2 \quad (2a)$$

$$A_3(f) = \frac{1}{2} \left\{ 1 - \cos \frac{\pi(f-f_2)}{2(f_3-f_2)} \right\} \quad f_2 \leq f \leq (2f_3 - f_2) \quad (2b)$$

$$A_3(f) = 1 \quad (2f_3 - f_2) \leq f \leq f_N \quad (2c)$$

where f_3 is the high-pass cut-off frequency. The medium-frequency band-pass filter is the complement of the other two filters:

$$A_2(f) = \frac{1}{2} \left\{ 1 - \cos \frac{\pi f}{2f_1} \right\} \quad 0 \leq f \leq 2f_1 \quad (3a)$$

$$A_2(f) = 1 \quad 2f_1 \leq f \leq f_2 \quad (3b)$$

$$A_2(f) = \frac{1}{2} \left\{ 1 + \cos \frac{\pi(f-f_2)}{2(f_3-f_2)} \right\} \quad f_2 \leq f \leq (2f_3 - f_2) \quad (3c)$$

$$A_2(f) = 0 \quad (2f_3 - f_2) \leq f \leq f_N \quad (3d)$$

Frequencies of 0.03 Hz, 0.06 Hz, and 0.15 Hz were used for f_1 , f_2 , and f_3 . Figure 1 contains graphs of the amplitude response of the three filters as a function of frequency. The time periods for the lower and upper cut-offs are 33.33 and 6.66 seconds, corresponding to spatial wavelengths of 250 km and 50 km.

Figure 2 shows an example of the results from filtering the RPA data. The top graph shows the original plasma density measurement; the bottom three traces show the signals which are output from the three filters. In this paper the most attention will be given to the fluctuations which are passed through the middle, band-pass filter. These fluctuations, with wavelengths of 50 to 250 km, will be referred to as "large-scale". The fluctuations measured with the high-pass filter, which have wavelengths of 10 to 50 km, will be referred to as "intermediate-scale". (The term "small-scale" will not be used since this is usually used to describe plasma variations with meter wavelengths.)

In Figure 3 is an example of plasma drift velocity data from the IDM which has been filtered in the same manner as the RPA data. Although the drift velocity is originally sampled at a much higher rate (32 Hz and 16 Hz) than the density measurements, for the purpose of this comparison the high-frequency data had been averaged and decimated to obtain a signal which is sampled at a frequency of 2 Hz.

The RPA density data from the band-pass filter (third plot from the top in Figure 2) show variations within the auroral zone which are co-located with some very prominent variations in the drift velocity (Figure 3). There does not appear to be a consistent phase correlation between the

1. *Introduction*

1

—

Digitized by srujanika@gmail.com

CONTENTS

¹⁰ See, for example, the discussion of the 1992 Constitutional Convention in the *Constitutional Convention of 1992: The Final Report* (1993).

19. *U. S. Fish and Wildlife Service, Biological Report 82(12): 1-100.*

1. *What is the relationship between the two variables?*

19. *Brachyponeranigrita* (Fabricius) (Fig. 10) is a common species throughout the region.

¹⁰ See, for example, the discussion of the 1992 Constitutional Convention in the *Constitutional Convention of 1992: The Final Report* (1993).

¹⁰ See, for example, the discussion of the 1992 Constitutional Convention in the *Constitutional Convention of 1992: The Final Report* (1993).

¹⁰ See, for example, the discussion of the 1992 Constitutional Convention in the *Constitutional Convention of 1992: The Final Report* (1993).

¹⁰ See, for example, the discussion of the 1992 Constitutional Convention in the *Constitutional Convention of 1992: The Final Report* (1993).

locations, the magnetic local time (MLT), invariant latitude (ILAT), and the magnetic activity K_p index for the time of the data receipt. There are 24 longitude bins, each one hour wide and centered on the hour. The invariant latitude is divided into 14 bins, each 2.5° wide, spanning the range from 60° to -30° . The magnetic activity is divided into only two bins: low activity ($K_p=0$ to 3+) and high activity ($K_p=4+$ to 9). The distribution of the data set is illustrated in Figures 6 and 7, which show the number of

minutes of data collected in each bin as a function of MLT and invariant latitude. The bin with the largest time for low activity conditions had 91 minutes of data. Unfortunately, the data distribution is less than ideal (i.e., non-uniform) as some of the very low and very high latitude bins have less than 14 minutes of data. There was considerably less data obtained under conditions of high activity ($K_p > 4-$); the bin with the most data had only 33 minutes and three low-latitude bins had no data at all.

Irregularity Distribution Maps

One survey conducted with this data set has consisted of counting the density enhancements which are passed through the band-pass filter, which has peak amplitude response at 0.06 Hz, corresponding to a wavelength of 124 km. Enhancements with widths of the order of 60 km are passed through this filter very efficiently. This width is of the same scale as the plasma "patches" or "blobs" measured with radar [Vickrey et al., 1980; Kelley et al., 1982]. The radar measurements show that plasma "blobs" with a latitudinal width of about 0.6° may extend vertically from an altitude of 300 km to over 600 km (the limit of the published radar figures). It is likely that the patches are extended upward as high as the HILAT orbital altitude.

Counting the blobs is a very simple procedure with the band-pass filtered data. The filter outputs are simple scanned to find negative to positive zero crossings which mark the beginning of blobs, and the next positive to negative transition marks the end of each blob. The maximum of the points between the beginning and end indicates the magnitude of each blob. The total number of density enhancements which were counted in the

data set with this technique was 42,149 for low geomagnetic activity and 15,104 for high activity. Plotting the distribution of all enhancements results in a somewhat random distribution, with a tendency for a higher number at the low-latitude dayside and a lower number in the nightside. But if only the patches with a magnitude greater than 10^3 cm^{-3} are counted, then definite patterns emerge. Figure 8 shows the distribution of 17,318 patches counted with low activity and Figure 9 shows the distribution of 7,714 blobs counted with high activity. These graphs have been normalized by dividing the number of blobs counted in each bin by the total time spent by HILAT within that bin, resulting in units of counts per minute.

This practice of selecting blobs on the basis of magnitude tends to favor those on the dayside where the background density is higher. As an alternative to measuring the absolute magnitude of the density enhancements, the relative magnitude ($\Delta n/n_0$) may be measured instead. The same procedure as before was followed in which the patches were counted by detecting the zero crossings of the band-pass filter output. The peak magnitudes were then divided by the background plasma density, as determined from the low-pass filter output. (Since DC offsets were subtracted from the data before the filtering, these offsets were added back to the low frequency signal to get the background density, n_0 .) Figures 10 and 11 show the results of selecting enhancements with $\Delta n/n_0$ greater than 0.05. The number of blobs selected by this criteria was 13,575 for low activity and 6,451 for high activity. If the selection cut-off is raised to 0.1, then the numbers are 4,854 and 2,809; Figures 12 and 13 show the graphs of the distribution of blobs using this higher cut-off value.

The same algorithm which had been used to map the density patches has

also been used to map the fluctuations in the plasma drift velocity (electric field) for the same time period, in order to serve as a frame of reference. These maps will show the location of the aurora under conditions of low and high magnetic activity. Figures 14 and 15 show the results of counting velocity fluctuations with magnitudes greater than 0.05 km-sec^{-1} . This velocity corresponds to an electric field magnitude of roughly 2 mV-m^{-1} . The number of fluctuations counted were 10,444 for low activity and 4,872 for high activity.

Spectral Slopes

The signals which are output by the band-pass filters have been used to determine the spectral slope of the plasma density and drift velocity irregularities. In order to derive values for average spectral slopes from the data base, the data base was scanned to find the times at which the satellite enters and leaves each MLT-ILAT bin. All data between the start and end times are squared and summed to determine power levels at two different frequencies. The spectral index is then computed as:

$$-S = \frac{\log P_2 - \log P_1}{\log F_2 - \log F_1} \quad (4)$$

Care must be taken in the calculation of the spectral indices in order to account for the shape and widths of the filter amplitude responses. The power levels (sum of output squared) from each filter are normalized by dividing by the filter bandwidth. The bandwidth is computed as the difference between the frequencies where the amplitude response is 1/2 (or

the Nyquist frequency, in the case of the high-pass filter). The values of F_2 and F_1 in Equation (4) are determined by a weighted average of the amplitude response:

$$F_n = \frac{\int_0^{f_N} f A_n(f) df}{\int_0^{f_N} A_n(f) df} \quad (5)$$

(The denominator in (5) happens to be equal to the filter bandwidth.) For the filter defined in Equation (3) the average frequency is 0.0956 Hz. For the filter defined in Equation (2) the average frequency is 0.5741 Hz for the IDM data and 0.44872 Hz for the RPA data (the difference being due to a higher Nyquist frequency in the IDM).

Processing of the entire data base results in a number of different measurements of the spectral index in each bin. All measurements in each bin are averaged in order to show how the spectral index changes with location and geomagnetic activity. Figures 16 and 17 show the resulting graphs of average spectral slope for the plasma drift velocity, and Figures 18 and 19 show the results for the plasma density.

Sharp boundaries which do not show up in the drift velocity data appear in the plasma density graphs, centered around local midnight. It was thought that these boundaries may be the result of a seasonal dependence, since the satellite sampled different local time zones at different times of the year. Figure 20 shows the average day of the year for the data in each bin; this graph casts further suspicion on the seasonal dependence, since sharp boundaries appear at the same locations as in Figure 19. In

order to test the hypothesis that the time of year affects the plasma density spectral slope, the average spectral slopes have been recalculated using data selected from different times of the year. Figures 21 and 22 show the results using spring data only (days 80 to 170), while Figures 23 and 24 show summer data (days 171 to 264). Figures 25 and 26 show data centered on the summer solstice (days 125 to 217), while Figures 27 and 28 show data from early spring and late summer (days 80 to 124 and days 218 to 264). The high values of the spectral slope (dark areas) which occur around midnight appear in every set of graphs. This contradicts the previous suspicion that the spectral index has a seasonal dependence.

III. Discussion of Results

The data shown here confirm the generally held belief that large-scale plasma enhancements are created in the auroral zone and are transported away from the production zone by convection. Enhancements in the number of large-scale plasma density "blobs" are seen in the auroral zone in Figures 8 through 13. The cusp region stands out in particular, especially between 12 and 15 hours MLT. Although the drift velocity (electric field) fluctuations graphed in Figures 14 and 15 show well-defined auroral ovals, the density variations extend beyond the auroral zone into regions where there are no corresponding electric field fluctuations. The patterns of the extended fluctuations are consistent with the transport of the blobs by the conventional two-cell convection pattern, which has anti-sunward flow over the polar cap. Plasma patches in the dayside are not seen equatorward of the auroral zone, as this would require movement upstream against the anti-

sunward flow. In contrast, the patches on the dayside do extend northward beyond the auroral zone, well into the polar cap, and they also extend southward of the auroral zone on the night side.

The spectral slopes of the drift velocity and plasma density are analyzed for two reasons. First, it can show if there is a correlation between the electric field and the plasma density, which might depend on wavelength. Second, the spectral slope indicates the relative power present at different scale-lengths, and might show how power is transferred from one scale-length to another.

The drift velocity spectral slope in Figure 16 shows a fairly well-defined pattern for low magnetic activity. An increase in the spectral slope in the auroral zone indicates an increase in the power being input to the system at the 50 to 250 km wavelengths which are passed by the middle filter. The night side tends to have a larger spectral slope than the dayside; the decreased conductivity seems to enhance the large-scale electric fields more than the small-scale electric fields. This trend is also seen in Figure 17, but the high activity data is somewhat disorganized.

The graphs for the plasma density spectral slope in Figures 18 and 19 show patterns with no resemblance to the electric field spectral slopes. This indicates that there is no one-to-one relationship between the density and electric field variations at these large, macroscopic scales. (At microscopic, i.e. centimeter, scales they are related.) The large-scale electric fields are driven by magnetospheric processes, while the plasma variations are linked to the ionosphere.

It is difficult to reach a firm conclusion from the graphs of plasma density spectral slope. The pattern in Figures 18 and 19 is surprising.

There is a very distinct increase in the spectral slope from 23 to 2 hours MLT. As mentioned earlier, the sharp boundaries look like they could be an artifact of a seasonal dependence imbedded in the data base. But the same sharp boundaries show up in each additional test with the data sorted by the time of year or length of day. Thus a change in the spectral slope with the season coupled with a seasonal bias in the data base does not seem to be the cause of the pattern seen on the ILAT-MLT plots, although this has not been established with a 100% certainty.

The high values of spectral slope indicate that the plasma irregularities measured with the high-pass filter (wavelength less than 50 km) are reduced in amplitude with respect to the irregularities with wavelengths of 50 to 250 km. Examination of the data indicates that the intermediate-scale fluctuations are damped in this region; the large-scale fluctuations do not have an increased amplitude here. The fact that these intermediate-scale fluctuations are damped here is a puzzle, since this region is where the ionospheric density and conductivity is the lowest. A low conductivity should increase the lifetime of the irregularities rather than promote their decay [Vickrey and Kelley, 1982].

There is another feature in the graphs of the density irregularity spectral slopes which should not be overlooked. The magnitude of the slope tends to be smaller on the dayside where the plasma density and ionospheric conductivity are larger. It may even change signs (marked as "underscale" on the graphs) so that the power is higher rather than smaller at the smaller wavelengths (higher frequency). It is possible that this could be an instrumental effect. Since the RPA does not function well when the plasma density is very low, it's response to the small-scale fluctuations

might not be independent of the ambient plasma density. Another factor which should be taken into consideration is the fact that HILAT is not orbiting directly within the ionosphere's F region but is flying above it. The degree to which measurements of plasma at 830 km altitude mirror the variations in the ionosphere may depend on both the ambient plasma density and the size of the variations. In other words, where the density is low the intermediate-scale fluctuations may not "couple" to the HILAT altitude as well as the large-scale fluctuations.

There is evidence from another experiment on HILAT which indicates that the pattern in Figures 18 and 19 is real. Basu et al. [1987] have made maps of the distribution of very small-scale ionospheric irregularities, as determined by the scintillations in the signal from the radio beacon. The most intense scintillations are found in the same region where the large spectral indices are measured. The instabilities which produce the small-scale irregularities and scintillations may feed on the intermediate-scale irregularities in the process. This would account for the apparent damping of the fluctuations measured with the high-pass filter.

IV. Summary

Six months of data from the plasma monitor instrument on the HILAT satellite have been used to map the distribution of large-scale plasma density irregularities in the high-latitude ionosphere. The variations in the drift velocity (electric field) have also been mapped for purposes of comparison.

The maps show that the largest concentration of the plasma patches is

within the auroral oval, which is also where the drift velocity irregularities are found. The largest concentration of blobs is within the dayside cusp region. The distribution of the blobs spreads out from the cusp into the polar cap, where there are no corresponding electric field fluctuations. It appears that the blobs are carried into the polar cap by convection. Blobs are also found equatorward of the auroral zone on the nightside but not on the dayside, which is consistent with transport by convection.

Although it has been stated that the plasma blobs appear to be produced in the same regions where the electric field fluctuations are found, it should be emphasized that the electric fields are not assumed to be the direct cause of the plasma blobs. Variations in the field-aligned currents (in both space and time) are the most likely source for the plasma blobs, and the electric field fluctuations simply show the locations of the current variations.

Maps of average spectral indices have also been drawn, based on the relative power measured at large (50 to 250 km) and intermediate (10 to 50 km) wavelengths. These graphs show that there is very little direct correlation between the large-scale electric field and plasma density variations.

The maps of spectral slope also show a very distinct steepening in the plasma density spectral slope in the evening side, from 23 to 2 hours MLT. This steepening indicates that the intermediate-scale fluctuations are being damped here. This same region is also known to produce the most intense radio scintillations. It appears that the intermediate-scale fluctuations are being consumed by the instability processes which produce the small-scale plasma which is responsible for the scintillations.

V. Acknowledgments

The author thanks Fred Rich and Sunanda Basu for valuable discussions about this research. This work was sponsored by the Air Force Geophysics Laboratory under contracts F19628-84-C-0126 and F19628-86-K-0045 with Regis College Research Center.

VI. References

Basinska, E. M., Development of software for the analysis of plasma measurements using the retarding potential analyzer, AFGL-TR-84-0372, 1984, ADA176890.

Fejer, B. G. and M. C. Kelley, Ionospheric Irregularities, Rev. of Geophys. and Space Phys., 18, 401-454, 1980.

Fremouw, E. J. and L. A. Wittwer, The HILAT satellite program: intruduction and objectives, John Hopkins APL Technical Digest, 5, 98-103, 1984.

Kelley, M. C., J. F. Vickrey, C. W. Carlson, and R. Torbert, On the origin and spatial extent of high-latitude F region irregularities, J. Geophys. Res., 87, 4469-4475, 1982.

Basu, Santimay, Basu, Sunanda Basu, E. MacKenzie, and D. Weimer, Ionospheric scintillations and in-situ measurements at an auroral location in the European Sector, in "Scattering and propagation in random media", AGARD-CPP-419, 50, 1987.

Potocki, K. A., The HILAT satellite, John Hopkins APL Technical Digest, 5, 104-108, 1984.

Rich, F. J. and R. A. Heelis, Preliminary data processing plan for the thermal plasma experiment on the HILAT satellite, AFGL-TR-83-0091, 1983, ADA132017.

Rich, F. J. et al., Cold plasma measurements on HILAT, John Hopkins APL Technical Digest, 5, 114-119, 1984.

Vickrey, J. F., C. L. Rino, and T. A. Potemra, Chatanika/TRIAD observations of unstable ionization enhancements in the auroral F-region, Geophys. Res. Lett., 7, 789-792, 1980.

Vickrey, J. F. and M. C. Kelley, The effects of a conductive E layer on classical F region cross-field plasma diffusion, J. Geophys. Res., 87, 4461-4468, 1982.

Vickrey, J. F., On the morphology of plasma density irregularities in the auroral F-region, Technical Report 1, Contract DNA001-81-0076, SRI International, 1982.

Weber, E. J. et al., Polar cap F layer patches: structure and dynamics, J. Geophys. Res., 91, 12,121-12,129, 1986.

VII. Figure Captions

Figure 1 Amplitude response curves of the three filters used to separate plasma density variations with different wavelengths.

Figure 2 Example of HILAT RPA plasma density data which has been filtered. The upper plot is the original unfiltered data. Below it, in order from top to bottom, are the plots of the signals from the low-pass, band-pass, and high-pass filters.

Figure 3 Example of HILAT IDM drift velocity data which has been filtered in the same manner as the plasma density. The format is the same as in Figure 2. Both figures are from the same station pass on the dayside. The component of ion drift which is measured is horizontal, perpendicular to the satellite track. This corresponds to the electric field along the satellite track, in the north-south direction.

Figure 4 Example of filtered plasma density data, in the same format as in Figure 2 but from a pass in the night side.

Figure 5 Drift velocity data from the same time period as Figure 4.

Figure 6 Distribution of all data collected with low magnetic activity.

In this graph and all subsequent figures the invariant latitude is divided into 14 bins which are 2.5° wide, spanning the range from 55° to 90° . There are 24 local time bins, each an hour wide. The plot shows the total number of minutes spent in each invariant latitude-MLT bin.

Figure 7 Distribution of all data collected with high magnetic activity.

Figure 8 Map of plasma density fluctuations with magnitude greater than 10^3 cm^{-3} , under conditions of low magnetic activity.

Figure 9 Map of plasma density fluctuations with magnitude greater than 10^3 cm^{-3} , under conditions of high magnetic activity.

Figure 10 Map of plasma density fluctuations with relative magnitude greater than 0.05, under conditions of low magnetic activity.

Figure 11 Map of plasma density fluctuations with relative magnitude greater than 0.05, under conditions of high magnetic activity.

Figure 12 Map of plasma density fluctuations with relative magnitude greater than 0.1, under conditions of low magnetic activity.

Figure 13 Map of plasma density fluctuations with relative magnitude greater than 0.1, under conditions of high magnetic activity.

Figure 14 Map of drift velocity fluctuations with magnitude greater than 0.05 km-sec^{-1} , under conditions of low magnetic activity.

Figure 15 Map of drift velocity fluctuations with magnitude greater than 0.05 km-sec^{-1} , under conditions of high magnetic activity.

Figure 16 Map of drift velocity spectral slope, under conditions of low magnetic activity.

Figure 17 Map of drift velocity spectral slope, under conditions of high magnetic activity.

Figure 18 Map of plasma density spectral slope, under conditions of low magnetic activity.

Figure 19 Map of plasma density spectral slope, under conditions of high magnetic activity.

Figure 20 Map which shows the average day of the year at which the data in each ILAT-MLT bin was collected by HILAT.

Figure 21 Map of plasma density spectral slope, under conditions of low magnetic activity, using only data from the spring equinox to the summer solstice.

Figure 22 Map of plasma density spectral slope, under conditions of high magnetic activity, using only data from the spring equinox to the summer solstice.

Figure 23 Map of plasma density spectral slope, under conditions of low magnetic activity, using only data from the summer solstice to the fall equinox.

Figure 24 Map of plasma density spectral slope, under conditions of high magnetic activity, using only data from the summer solstice to the fall equinox.

Figure 25 Map of plasma density spectral slope, under conditions of low magnetic activity, using only data centered around the summer solstice.

Figure 26 Map of plasma density spectral slope, under conditions of high magnetic activity, using only data centered around the summer solstice.

Figure 27 Map of plasma density spectral slope, under conditions of low magnetic activity, using data only from early spring and late summer.

Figure 28 Map of plasma density spectral slope, under conditions of high magnetic activity, in early spring and late summer.

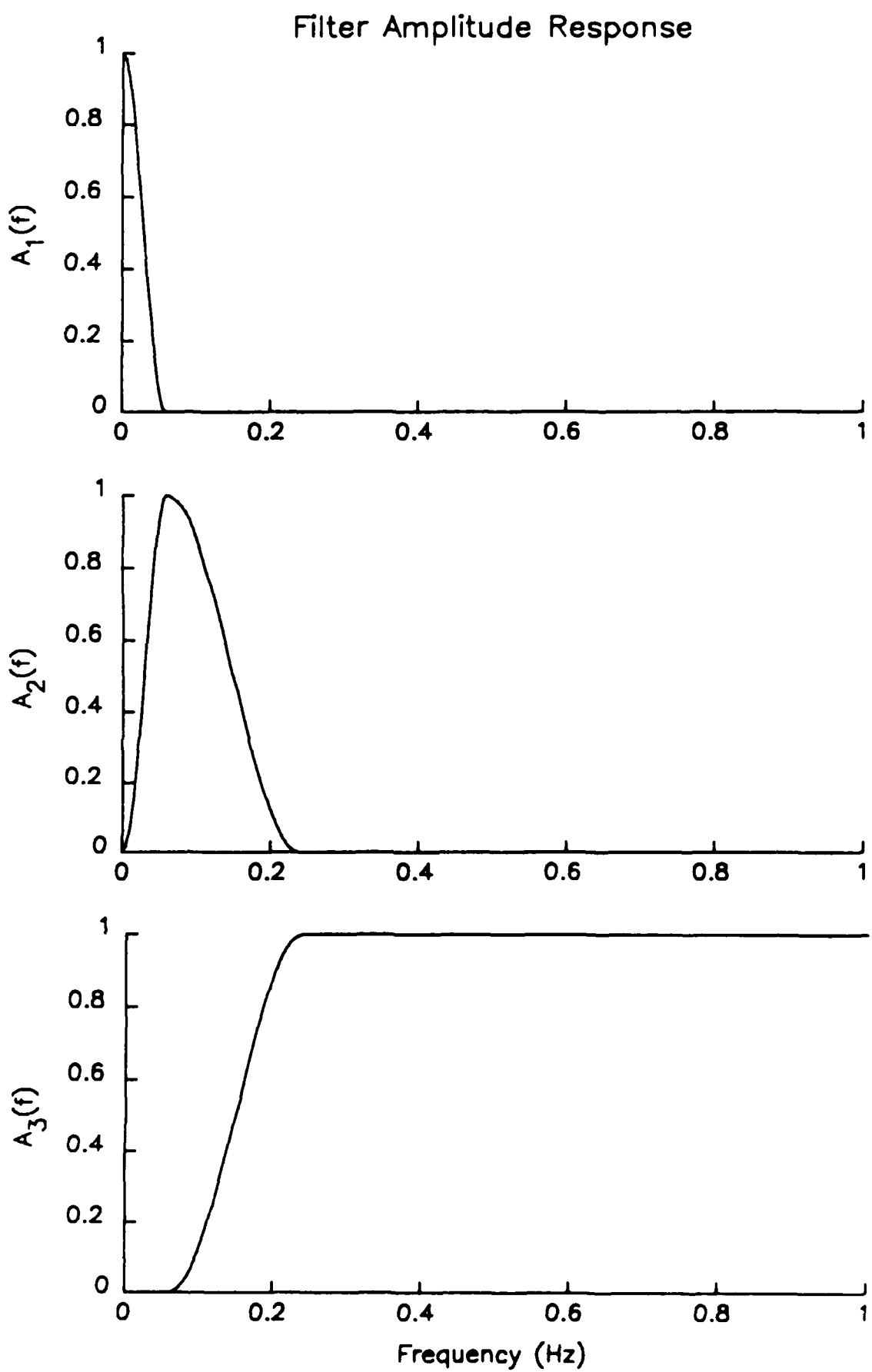


FIGURE 1

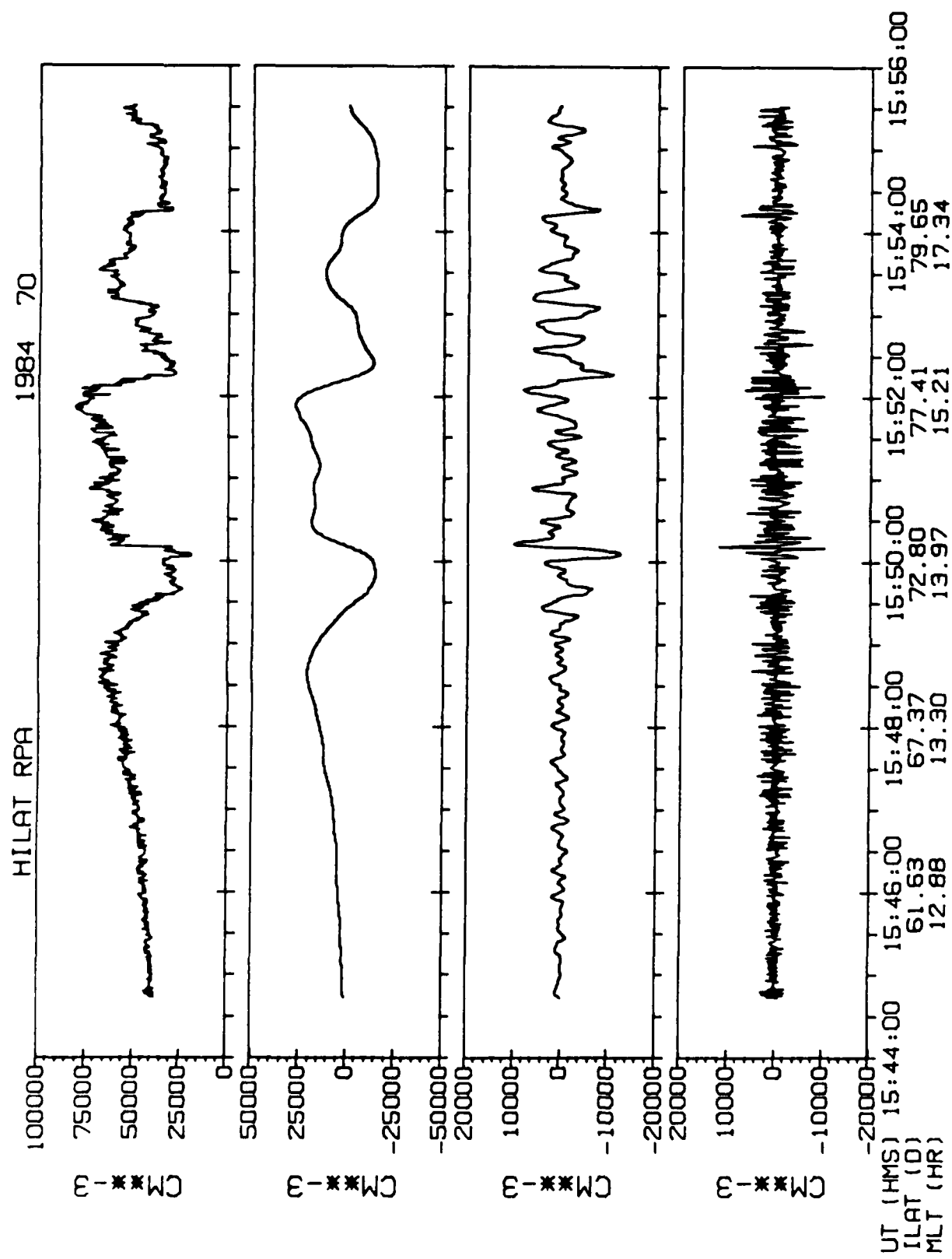


FIGURE 2

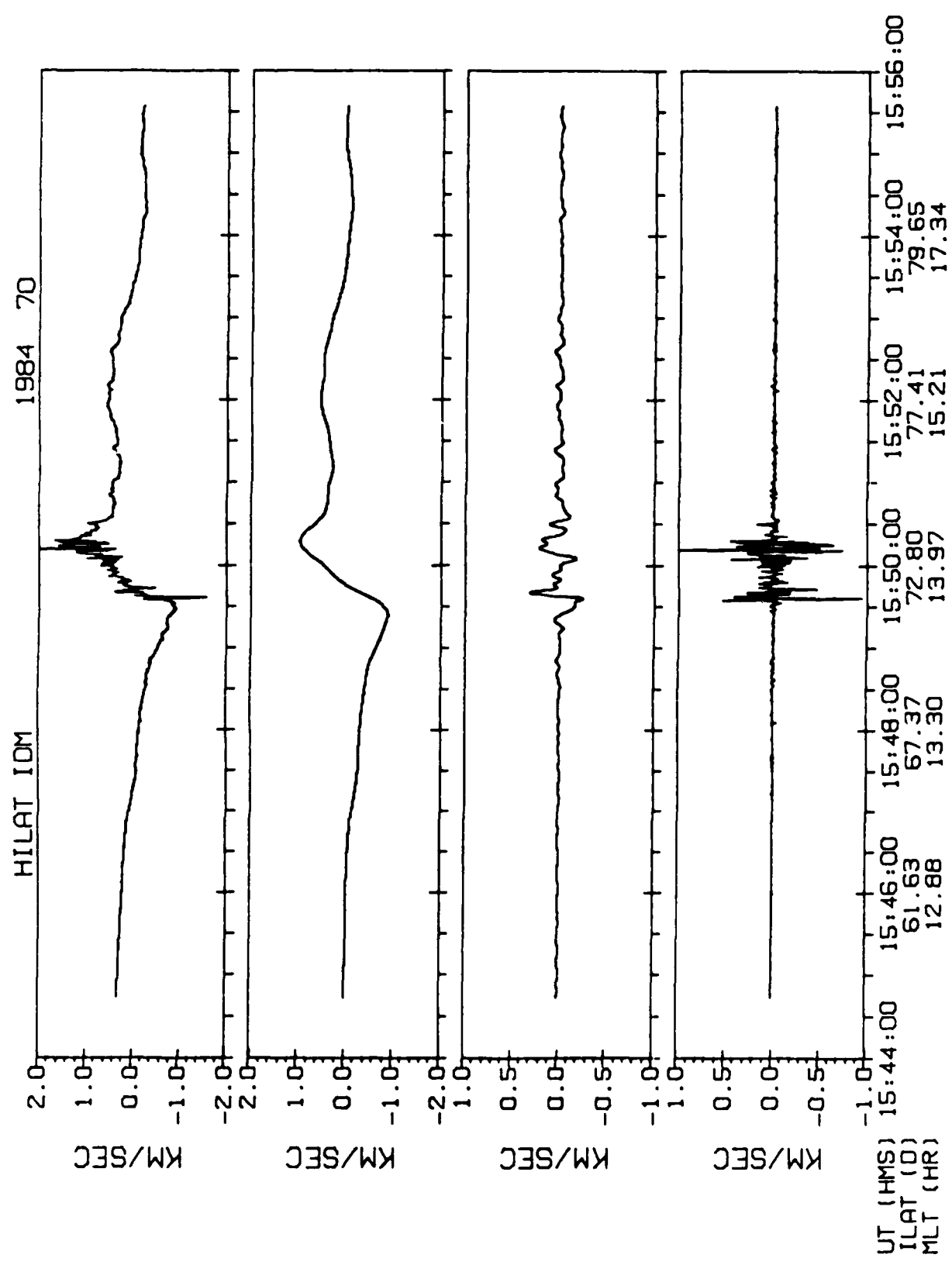
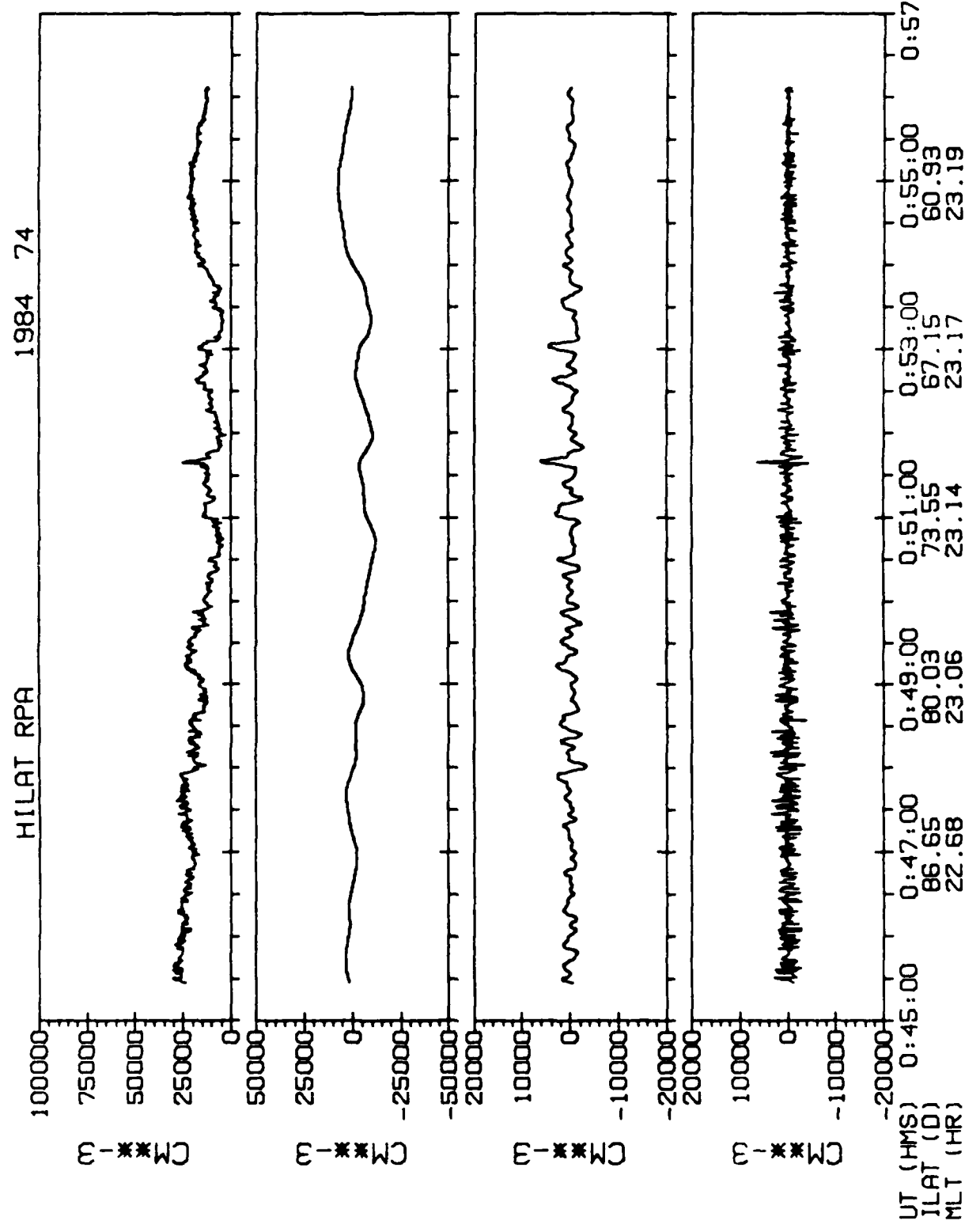


FIGURE 3



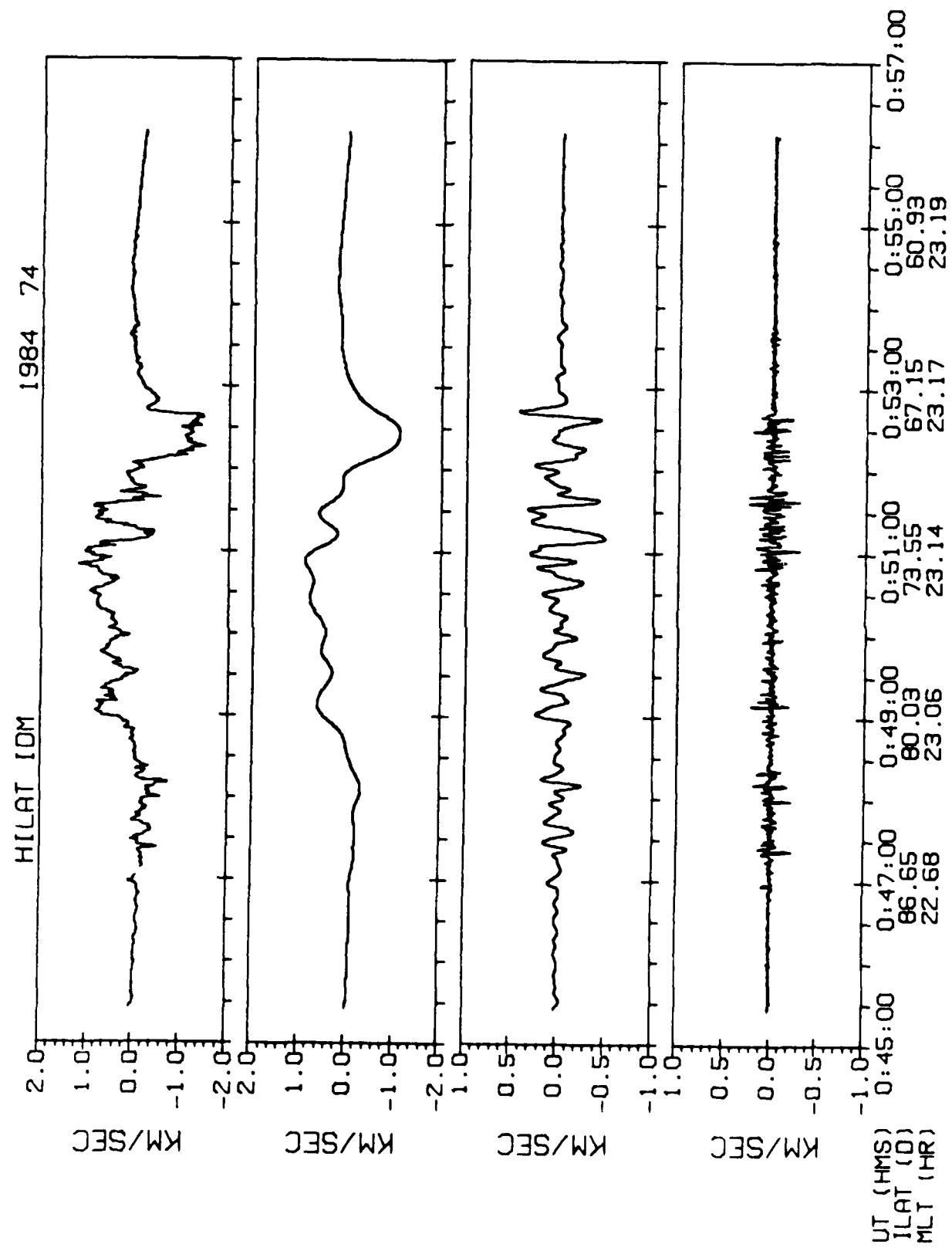


FIGURE 5

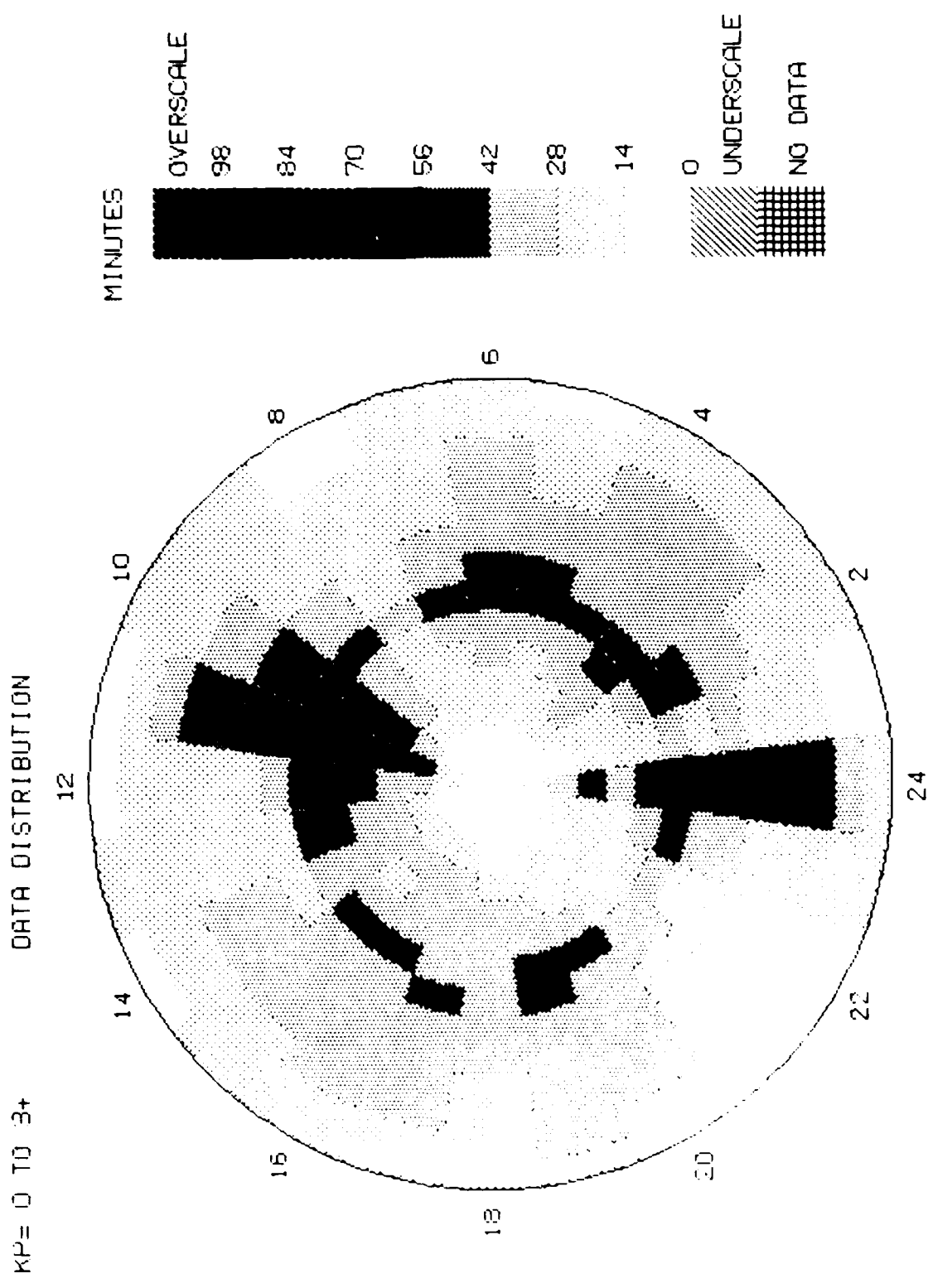


FIGURE 6

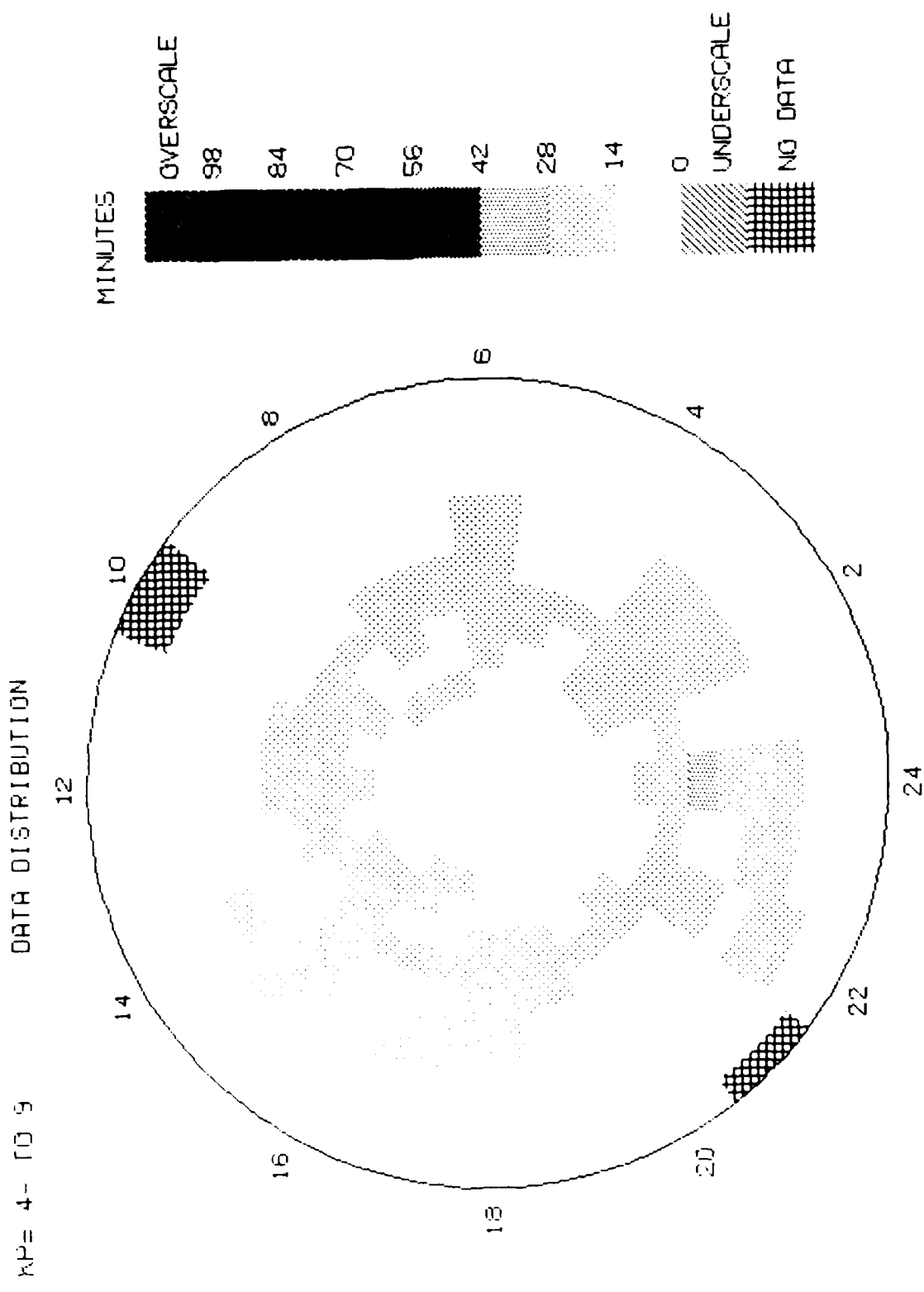


FIGURE 7

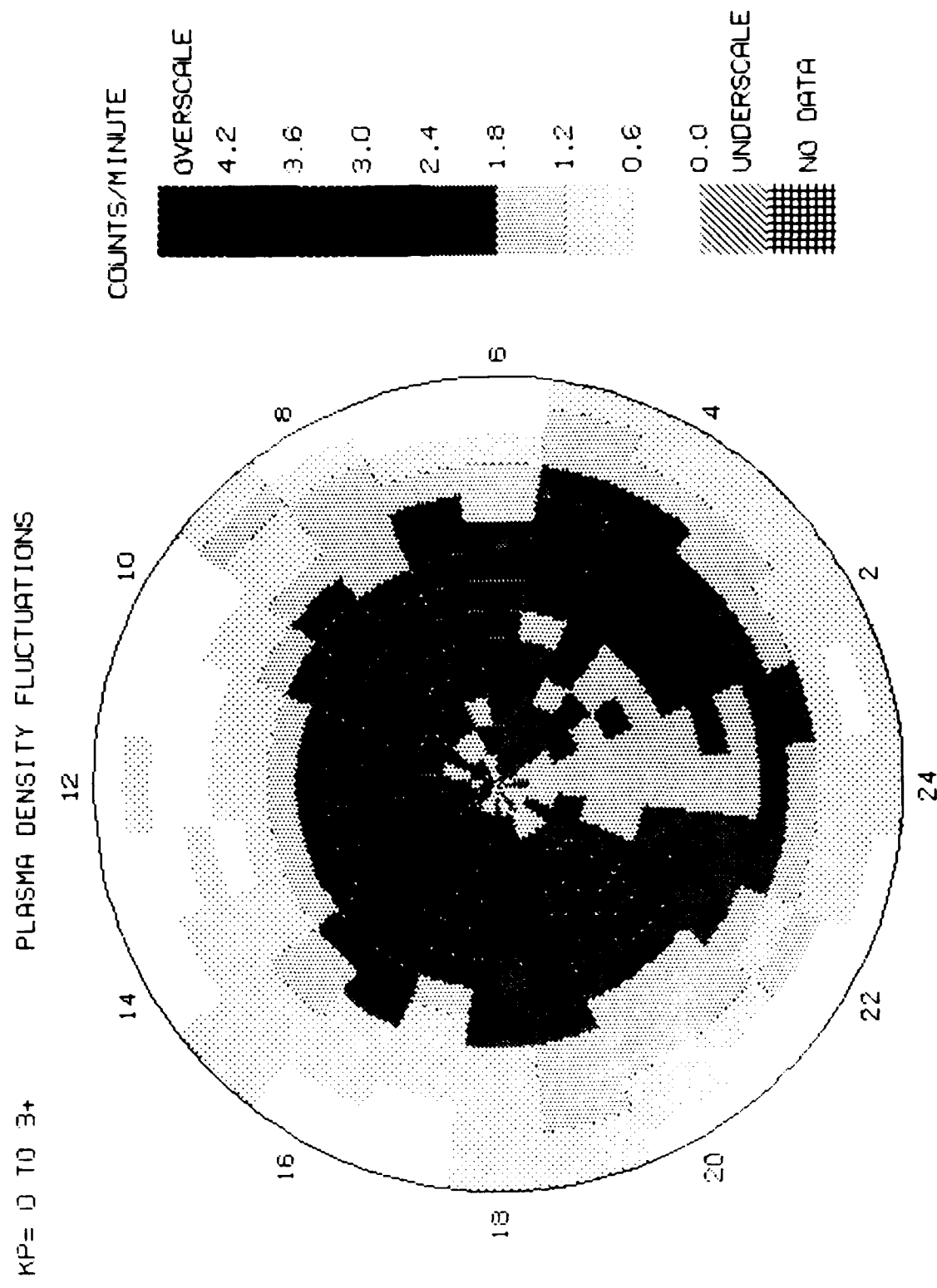
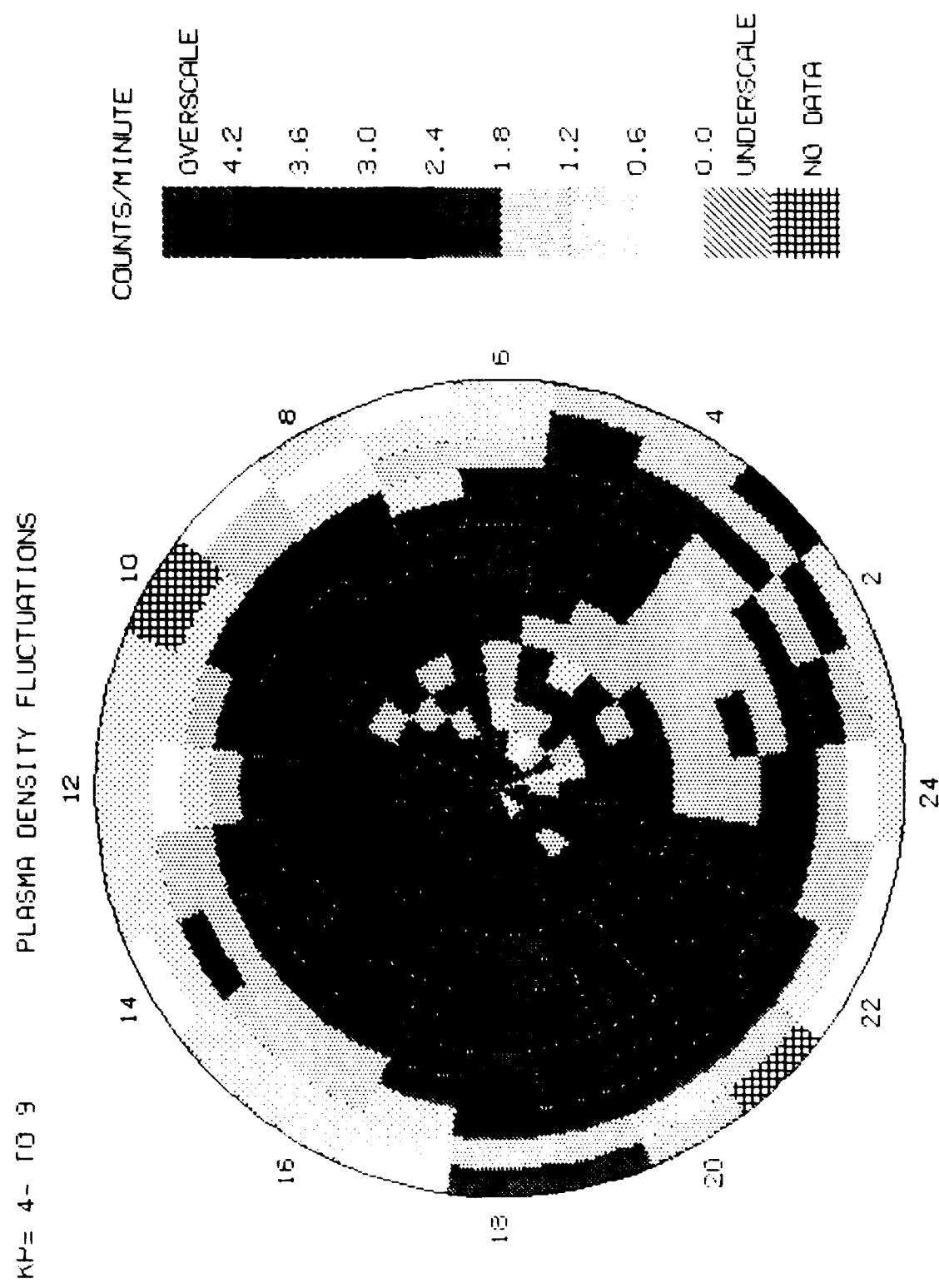
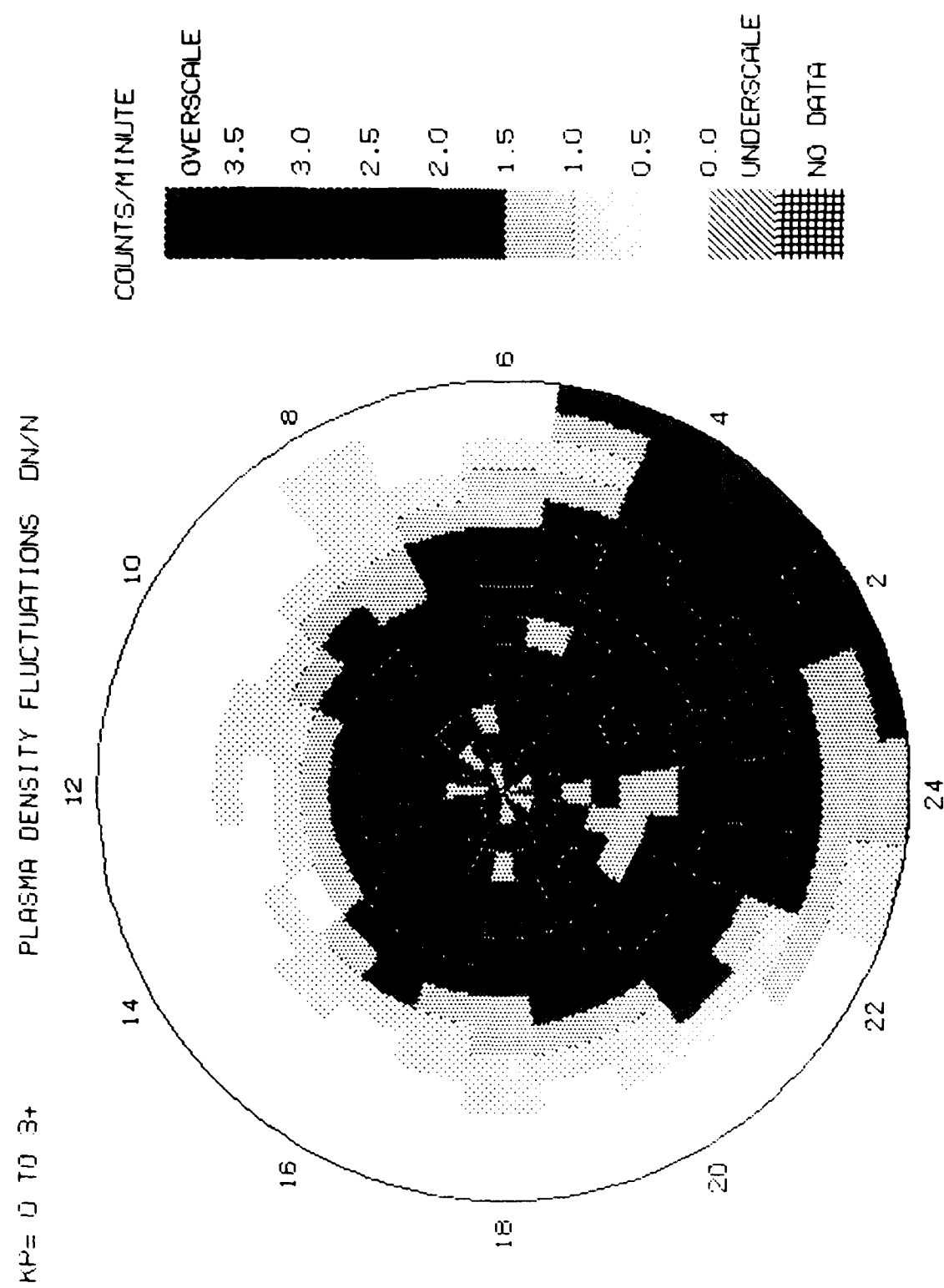


FIGURE 8





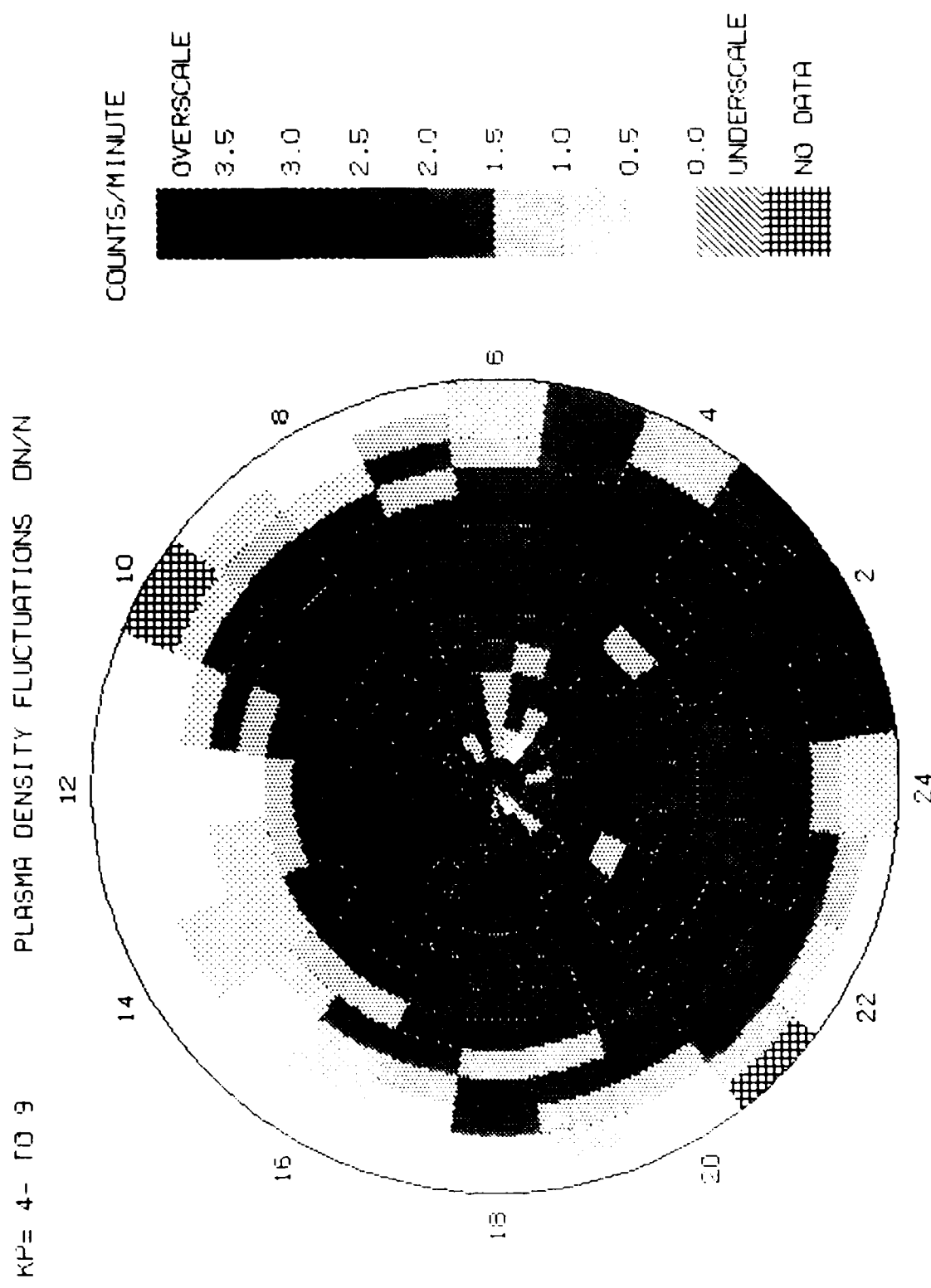
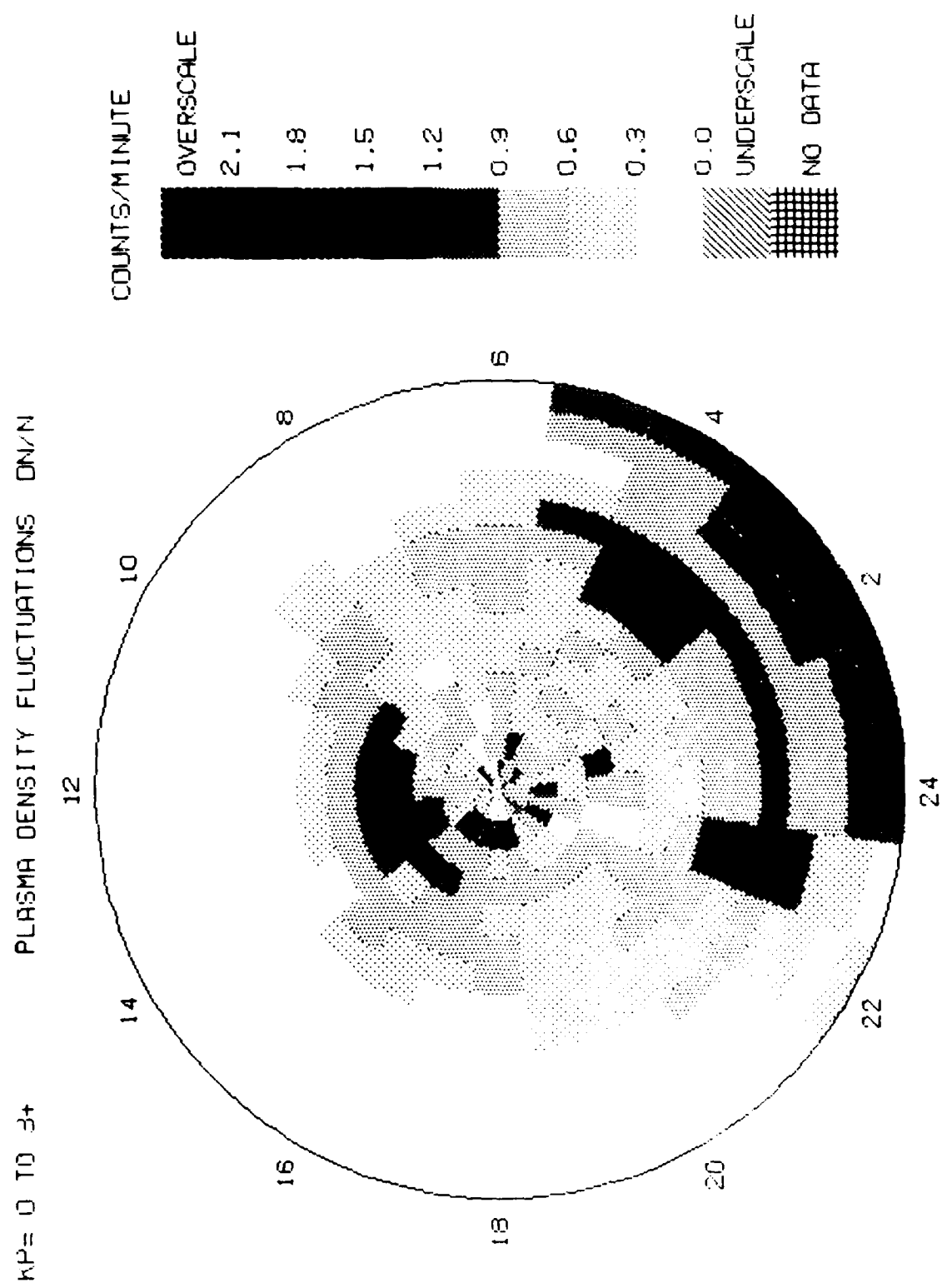


FIGURE 11



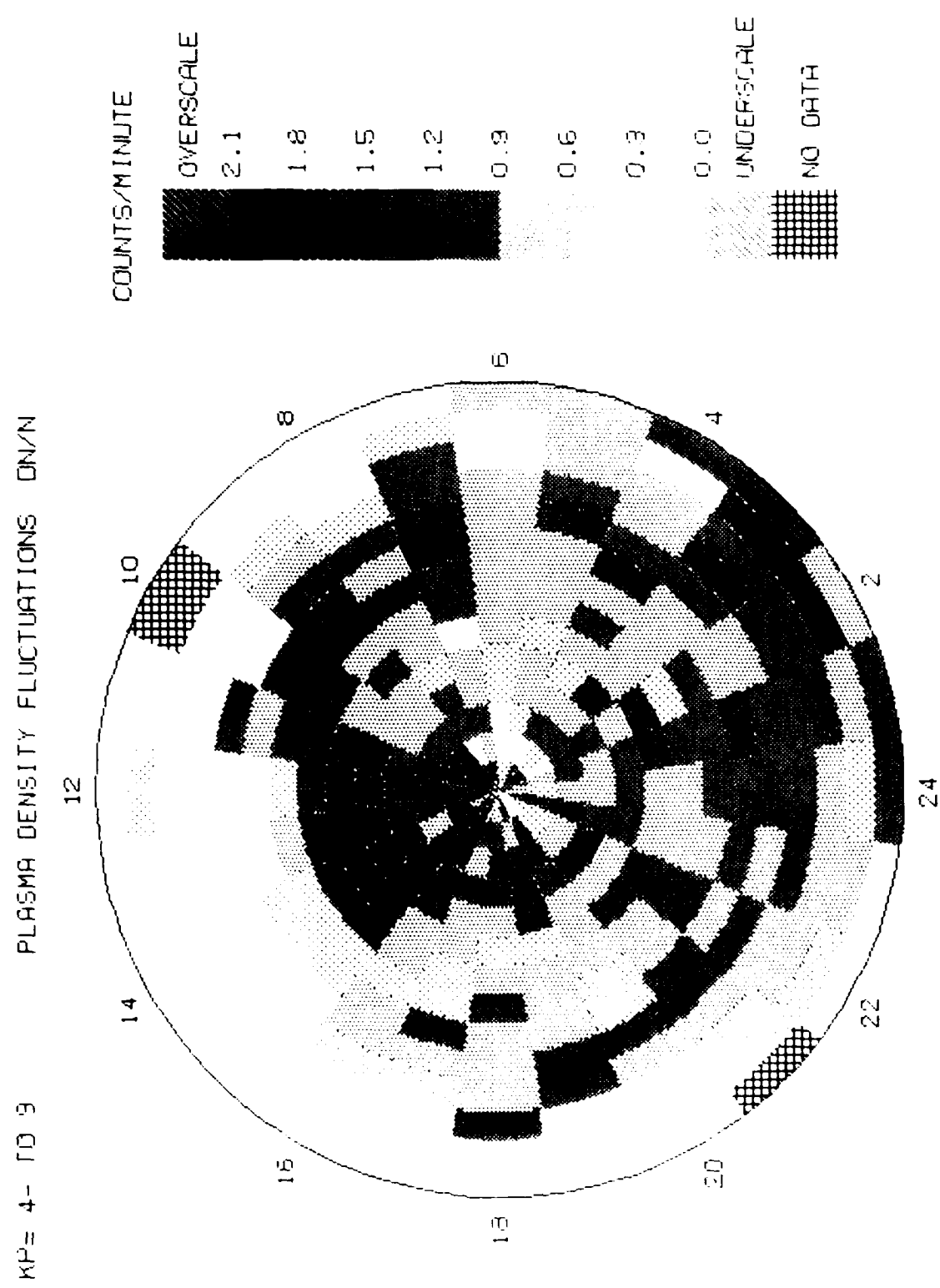


FIGURE 13

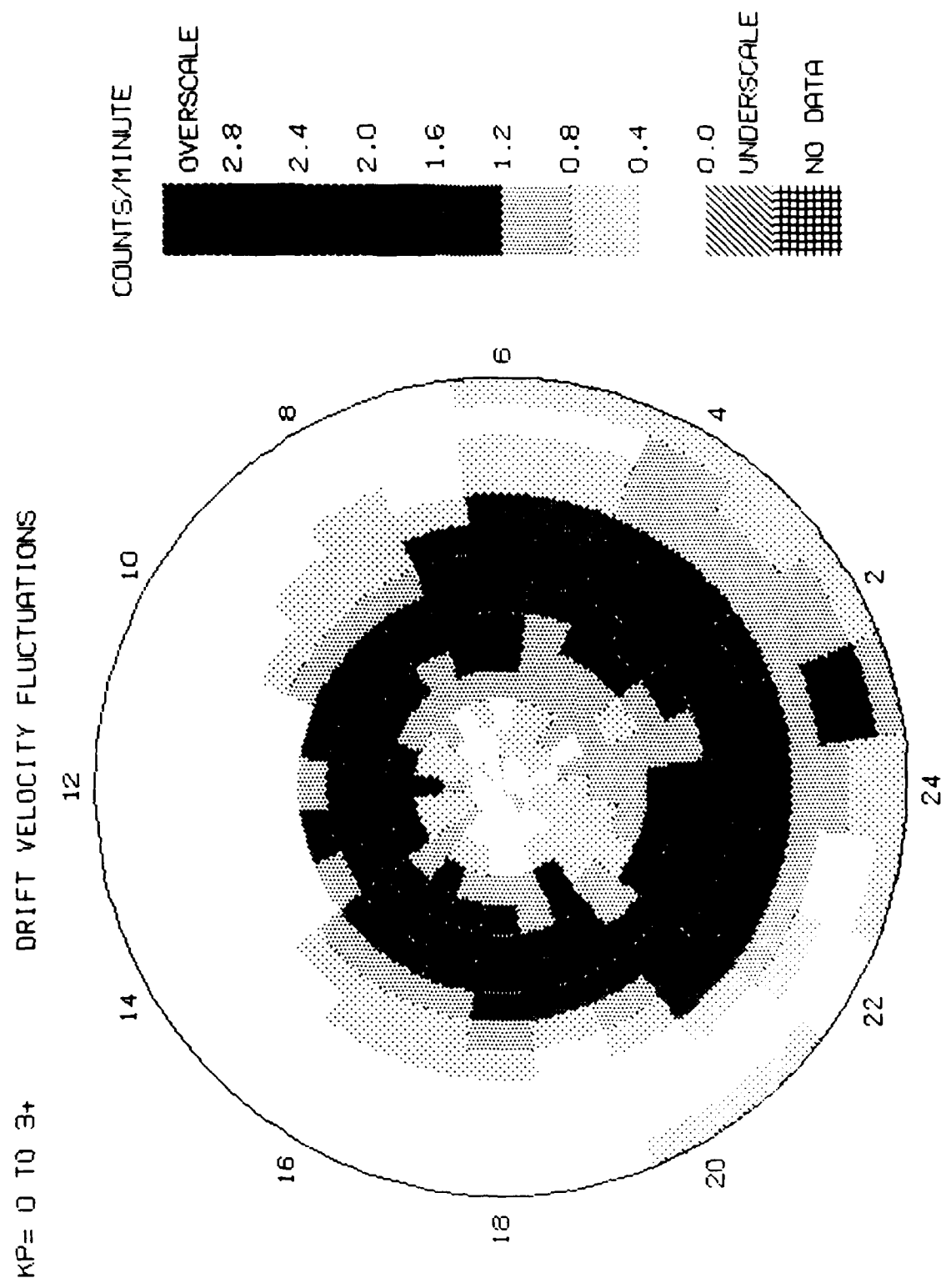


FIGURE 14

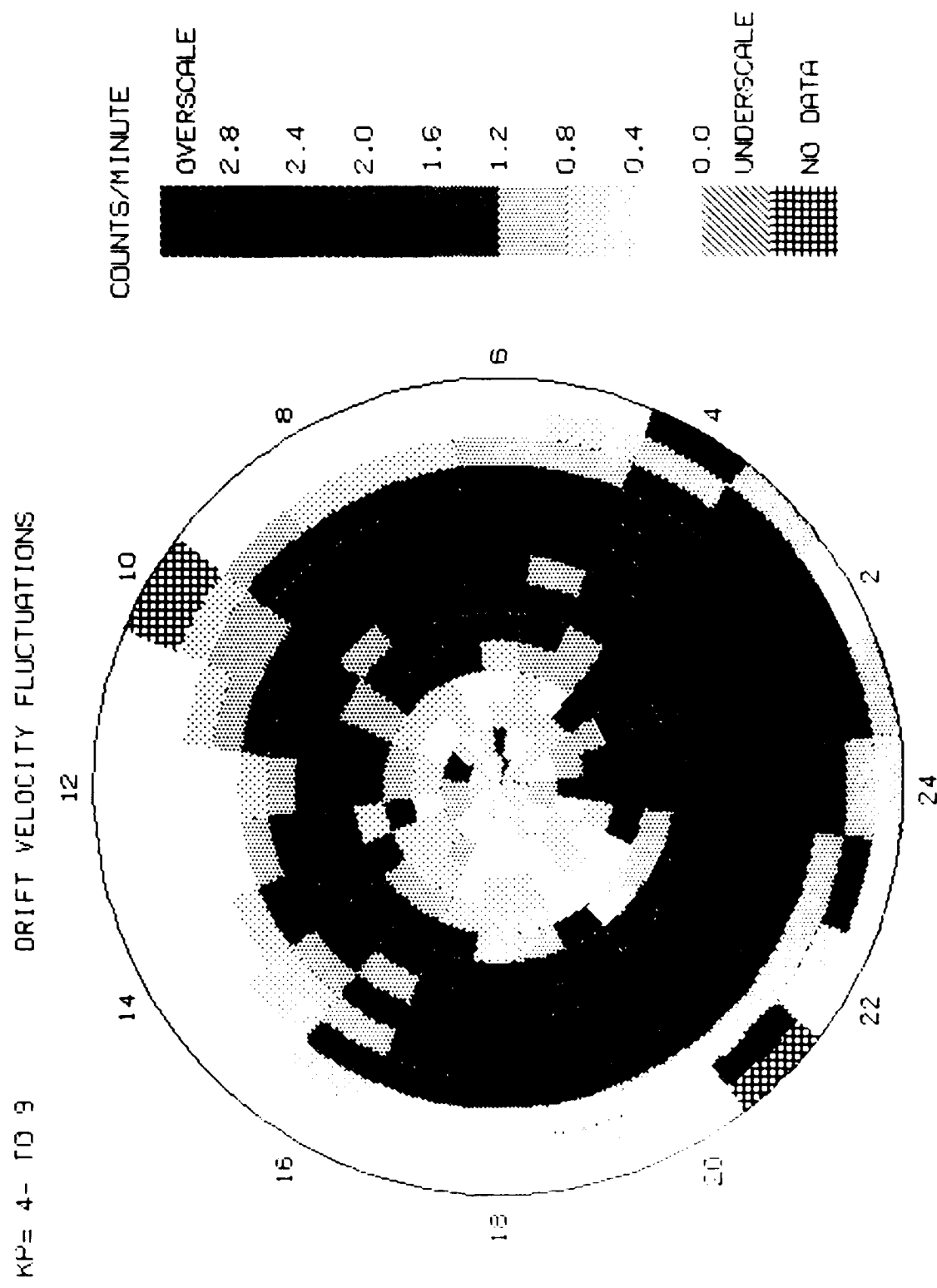
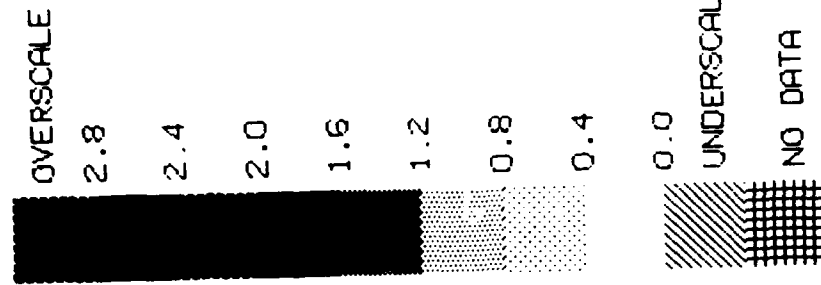
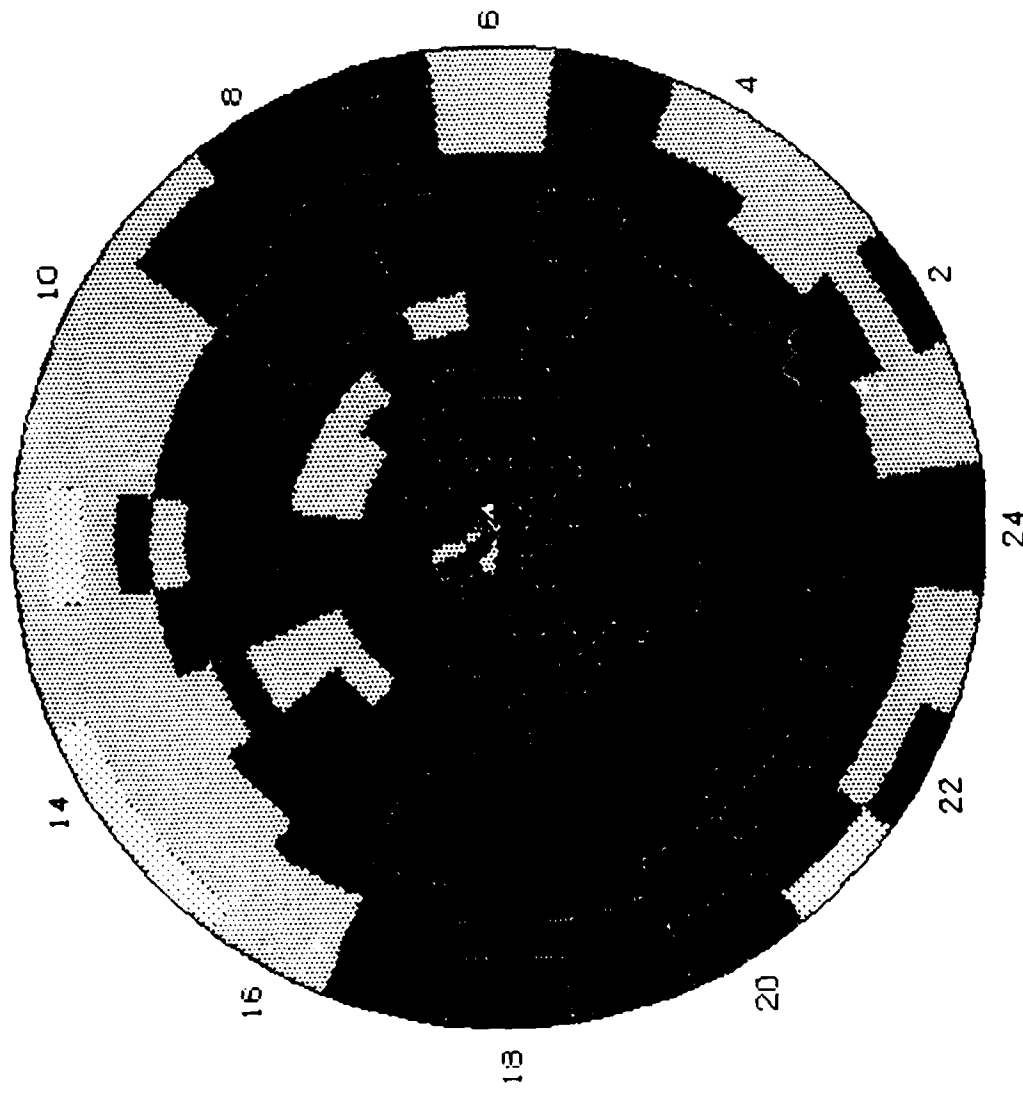
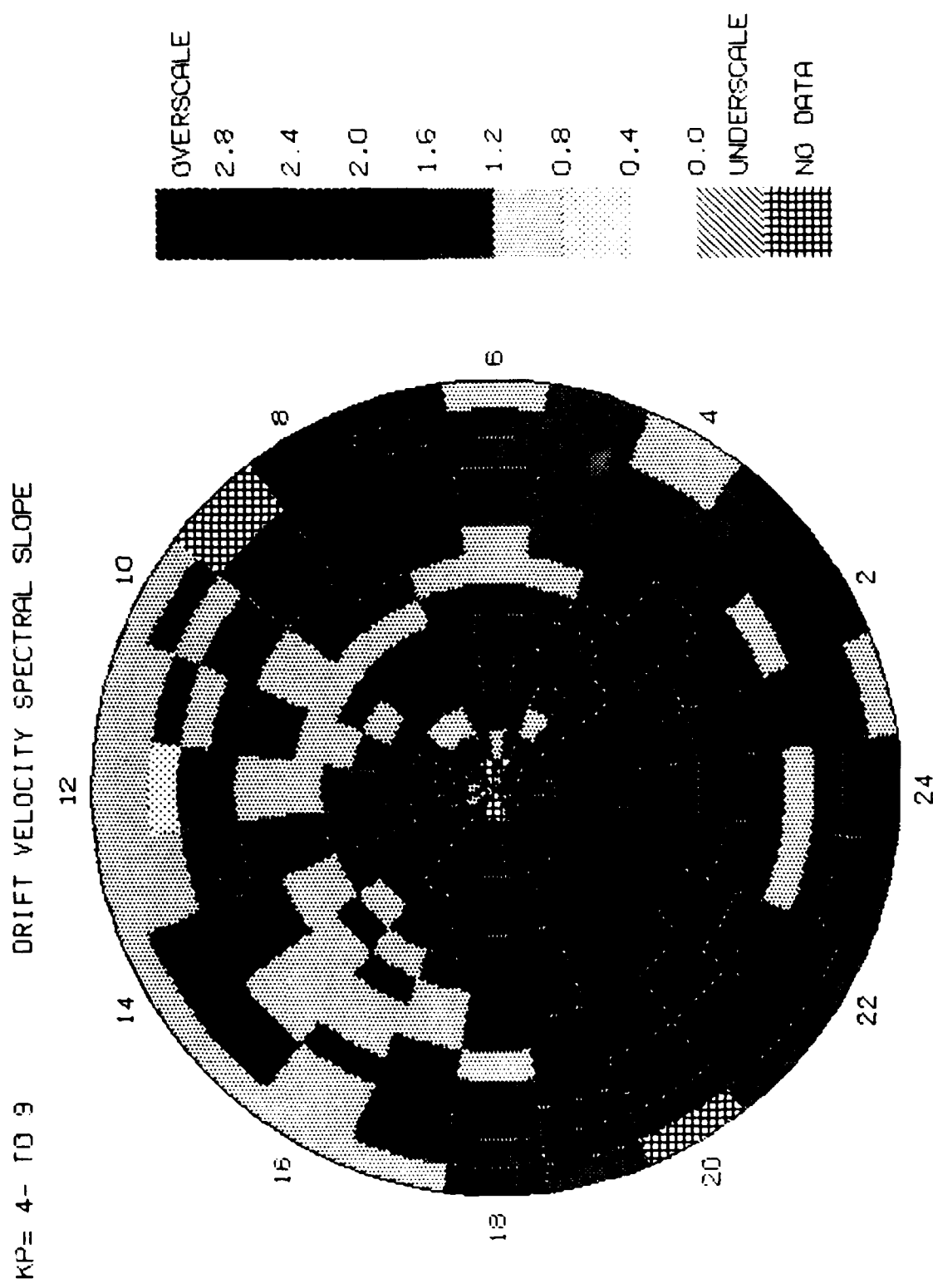


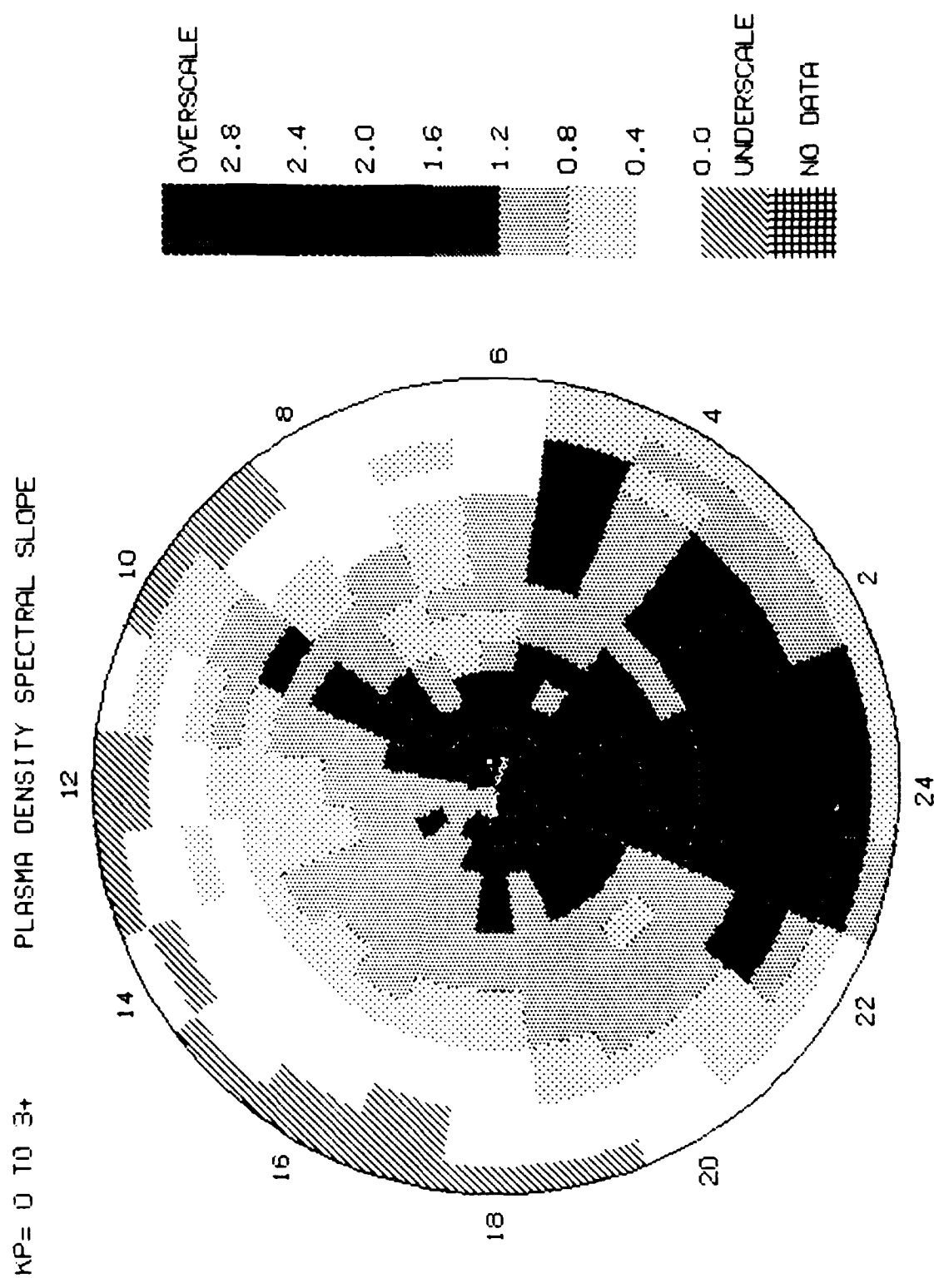
FIGURE 15

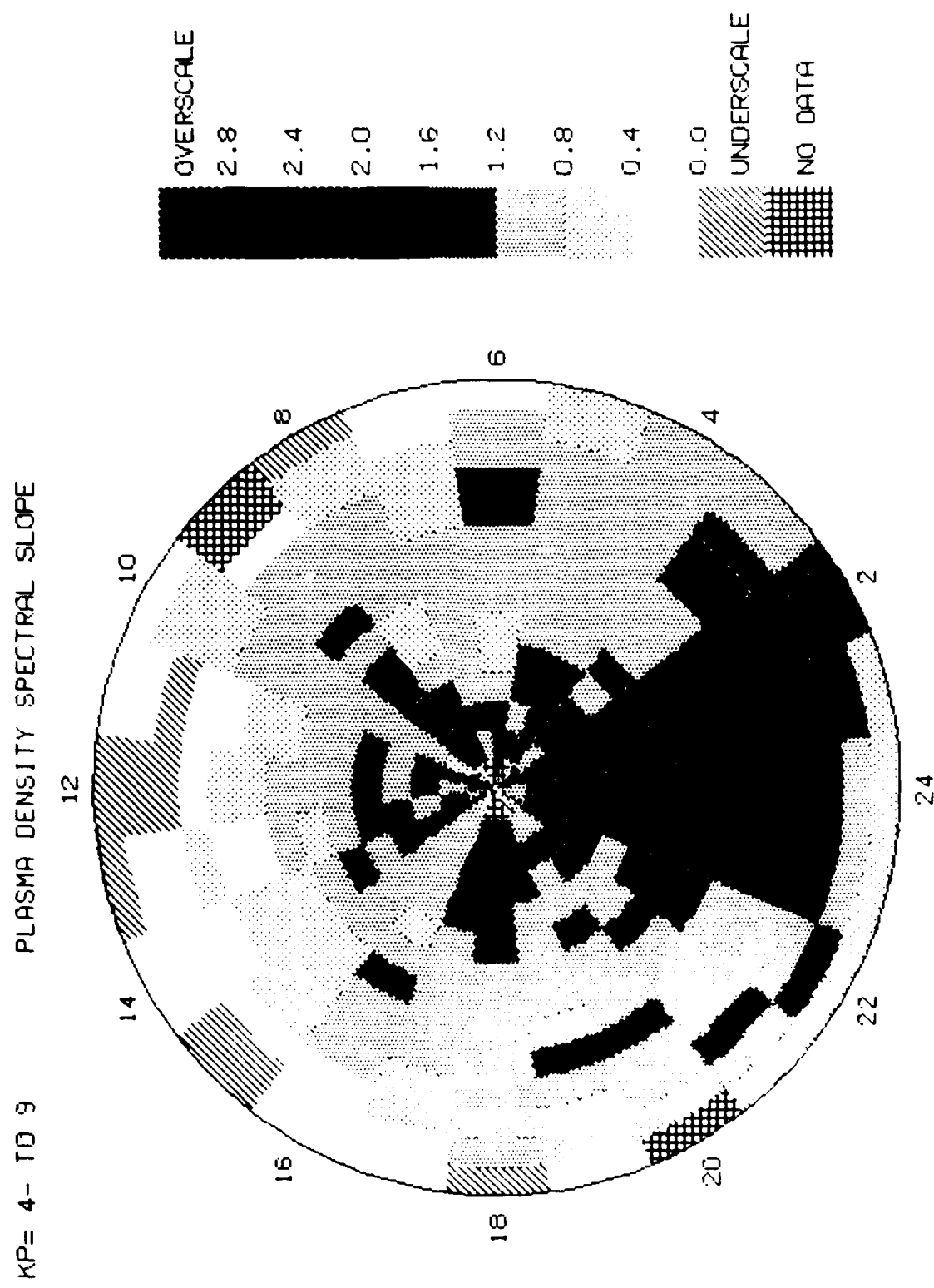
KP = 0 TO 3+

DRIFT VELOCITY SPECTRAL SLOPE









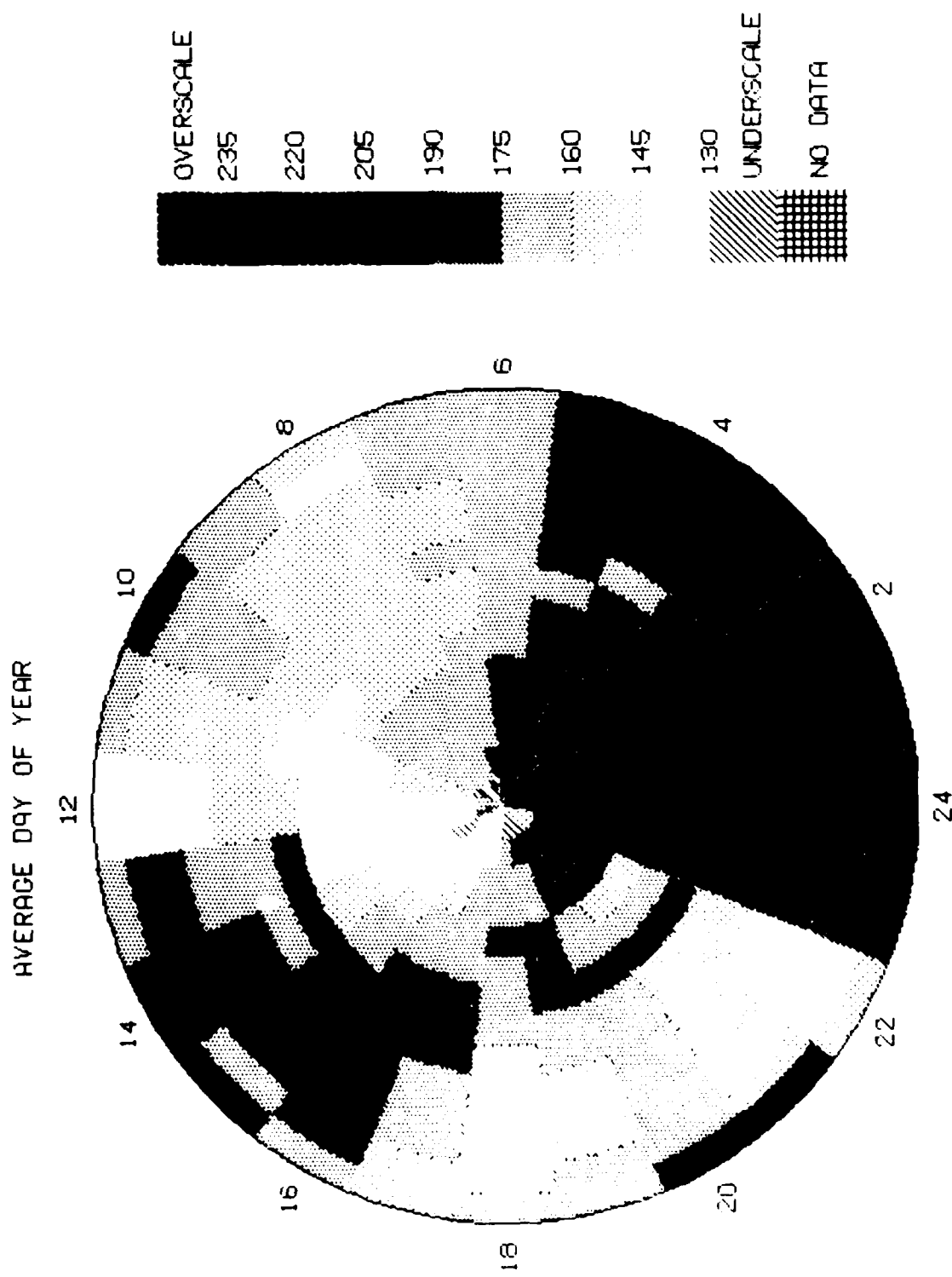
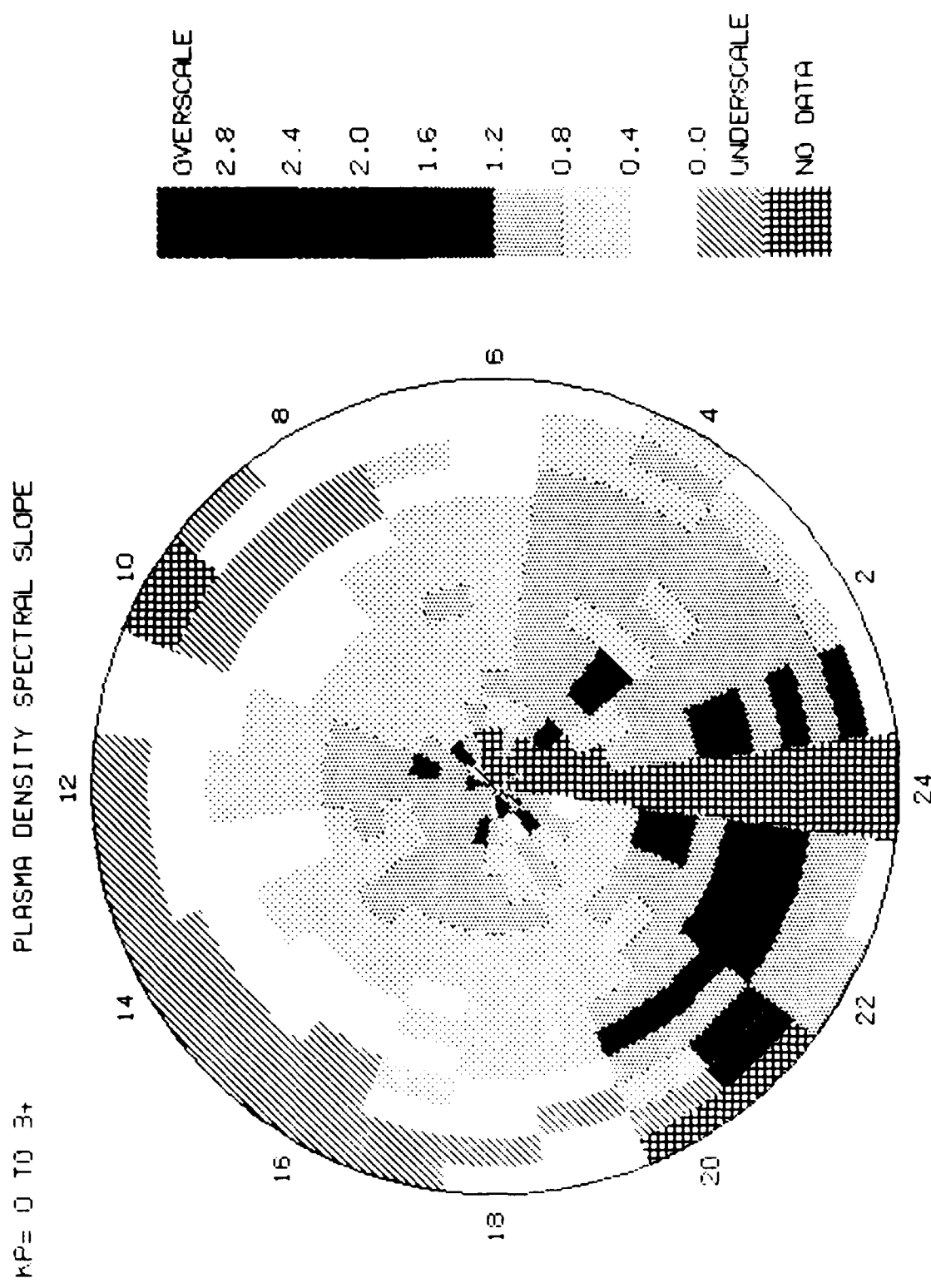


FIGURE 20



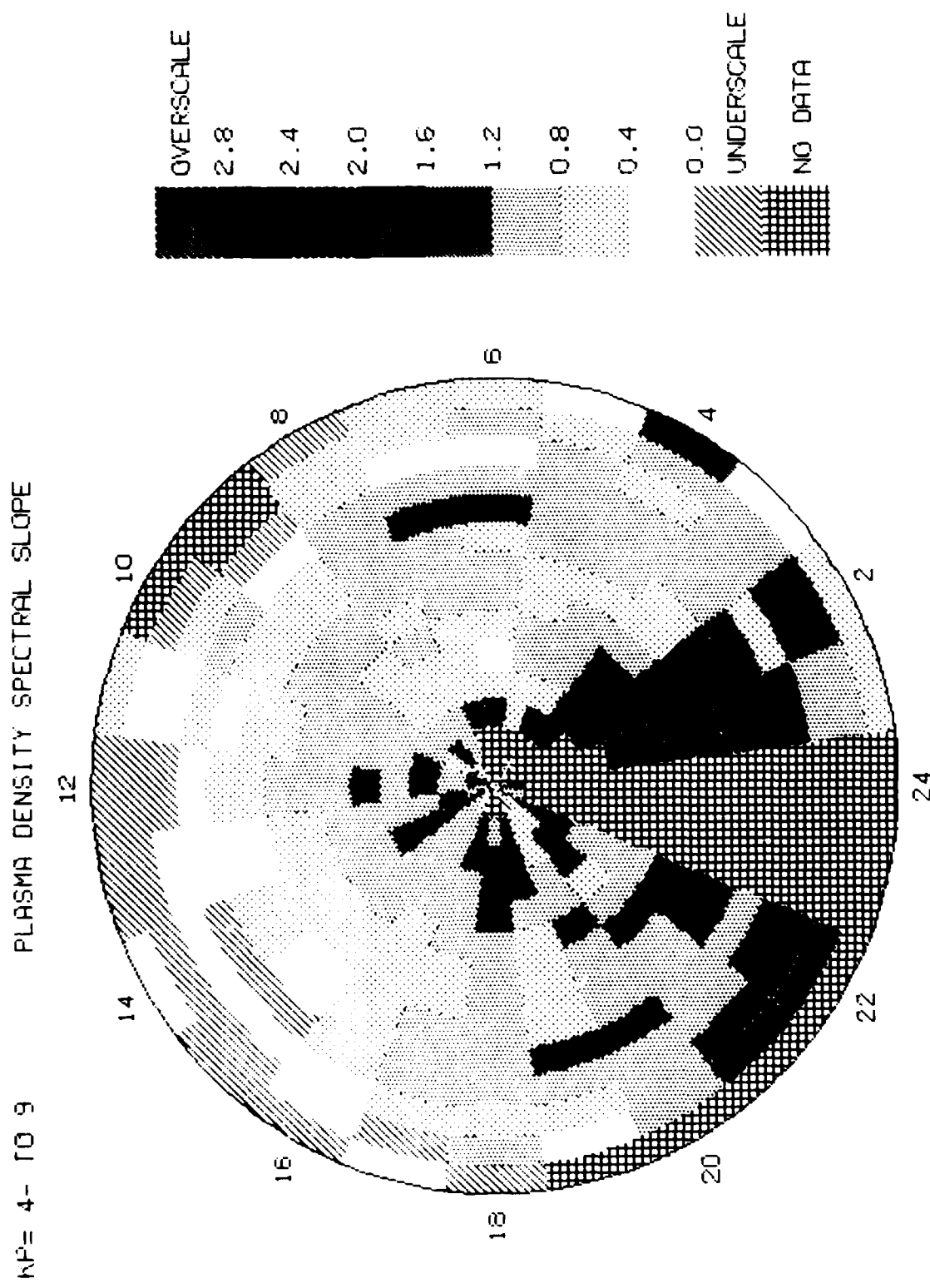


FIGURE 22

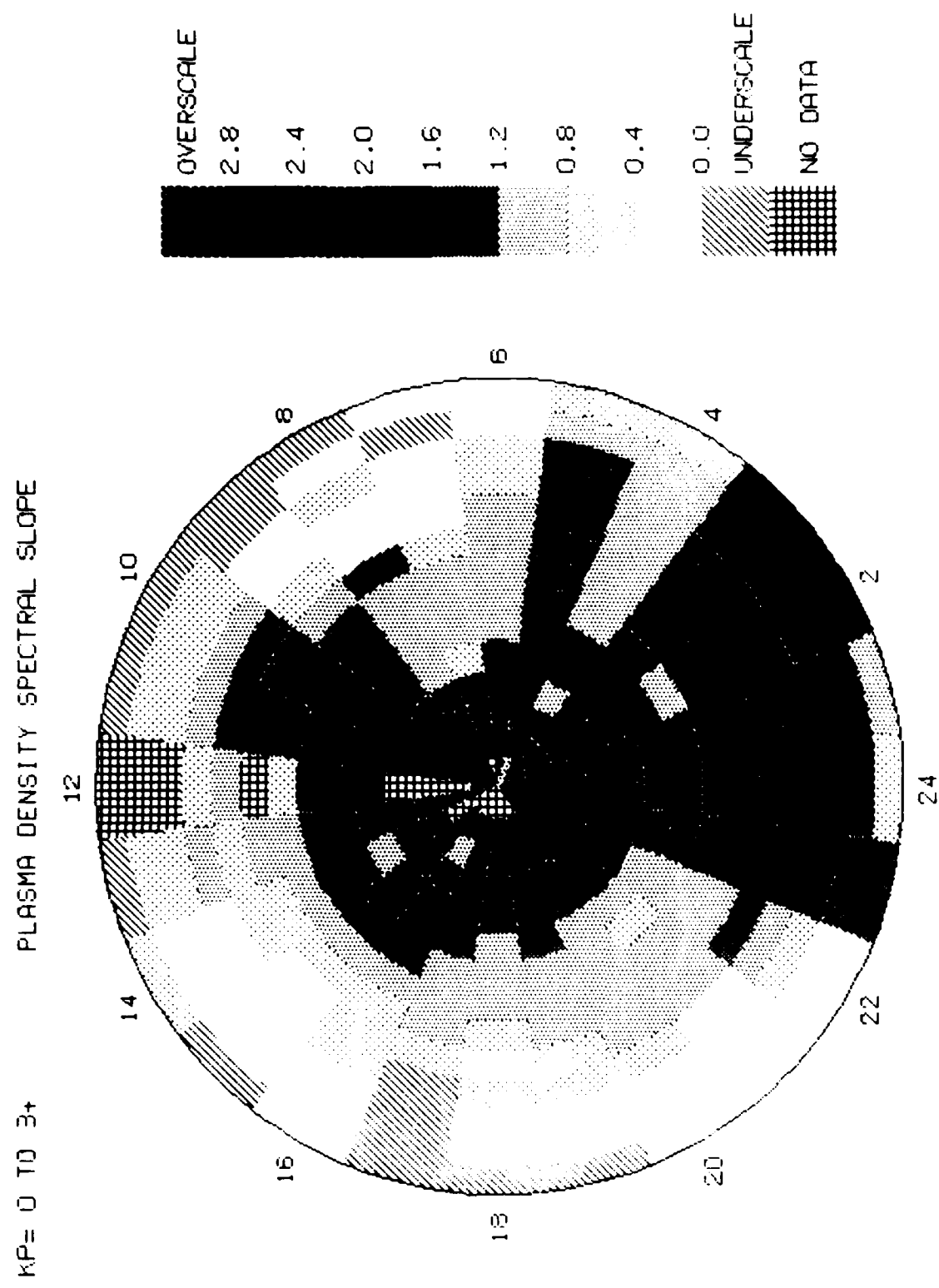


FIGURE 23

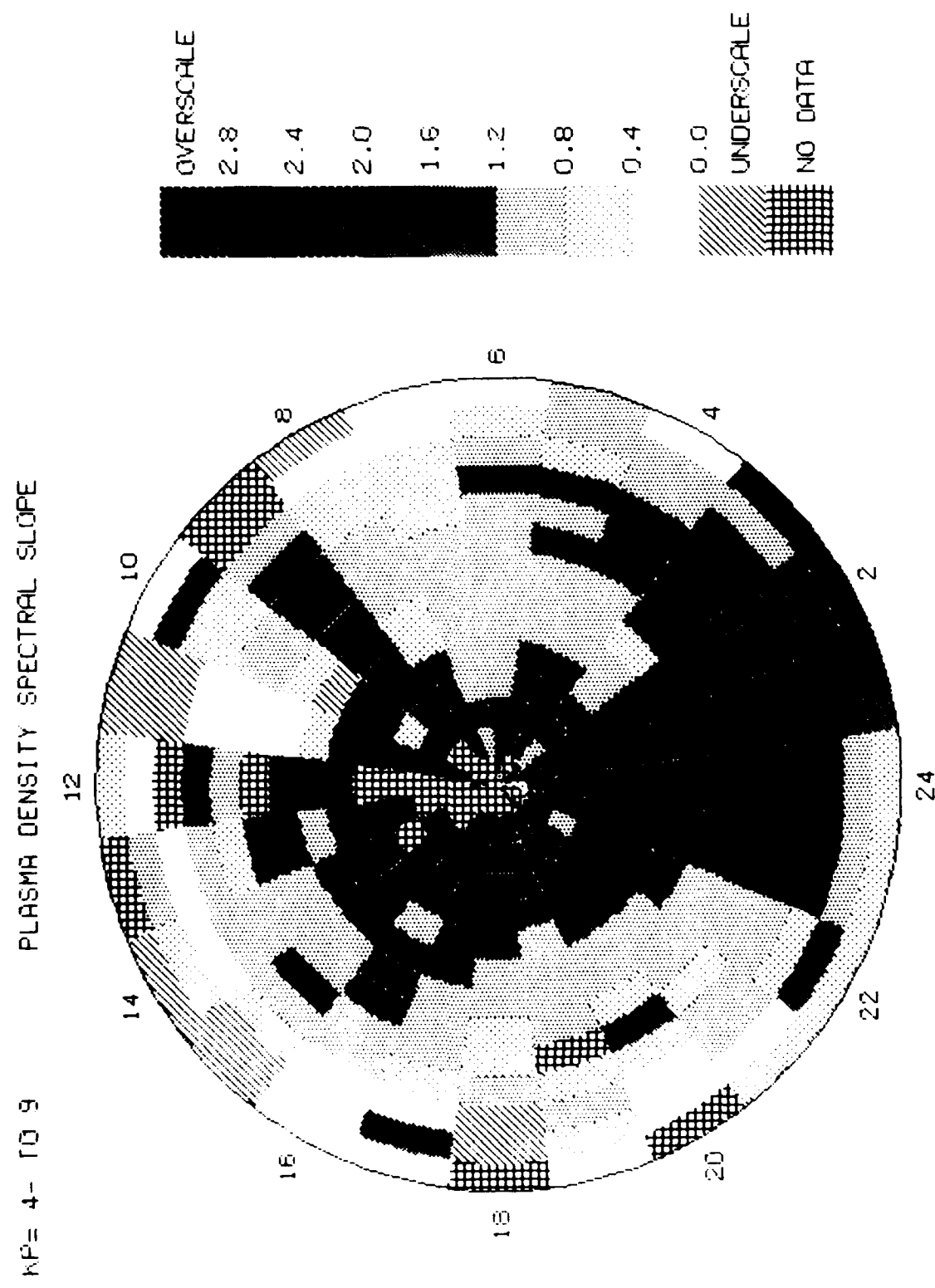
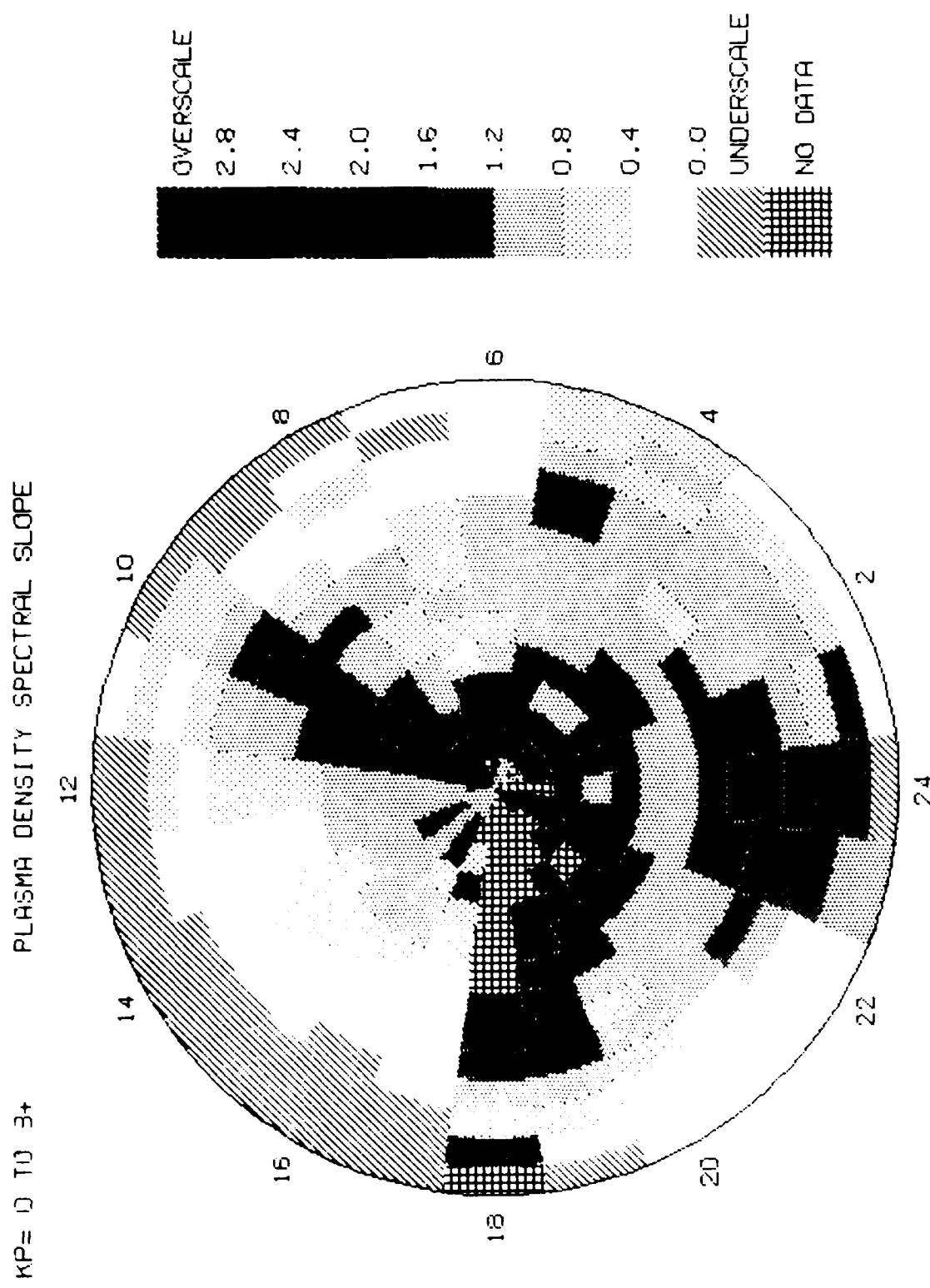
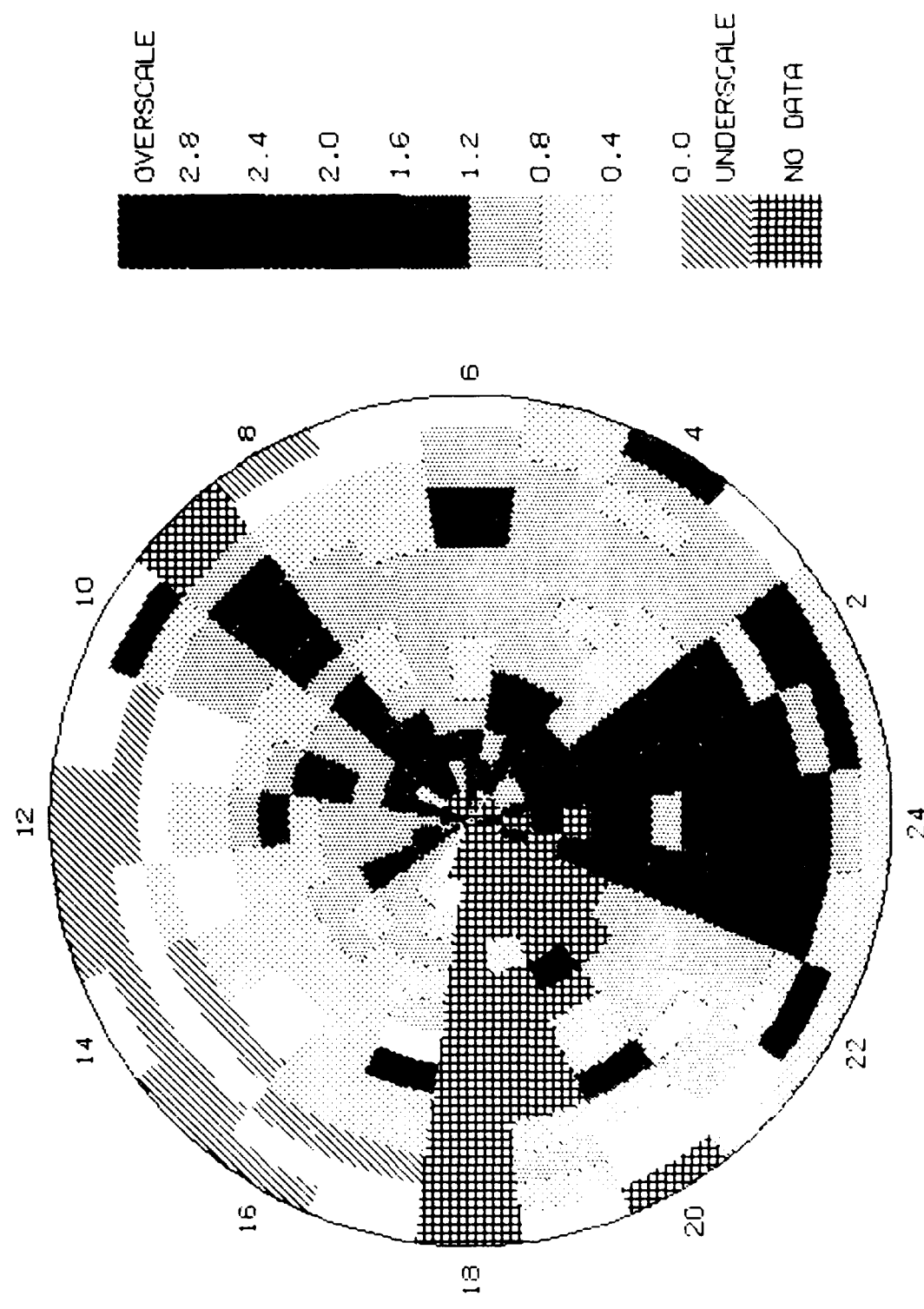
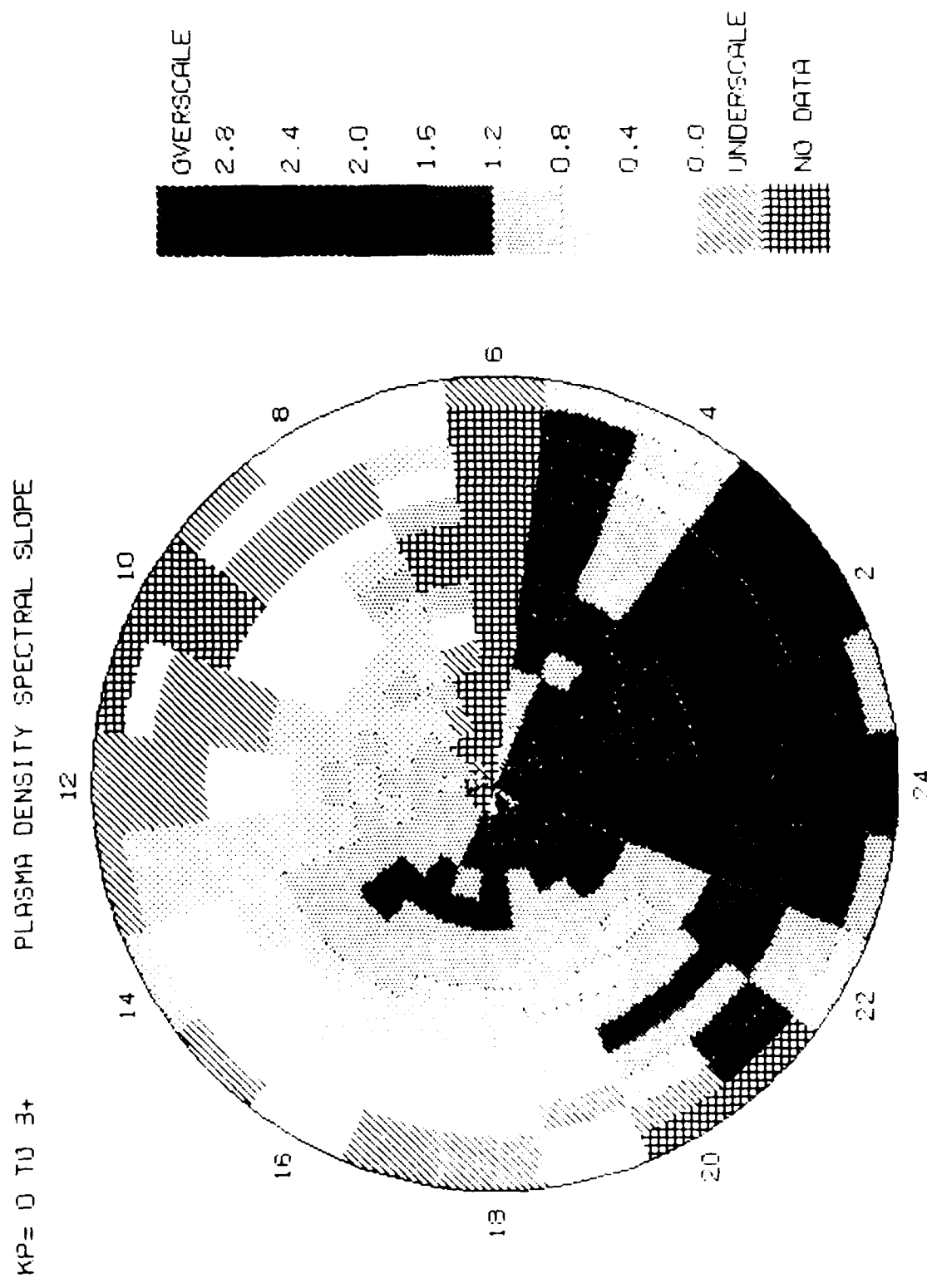


FIGURE 24



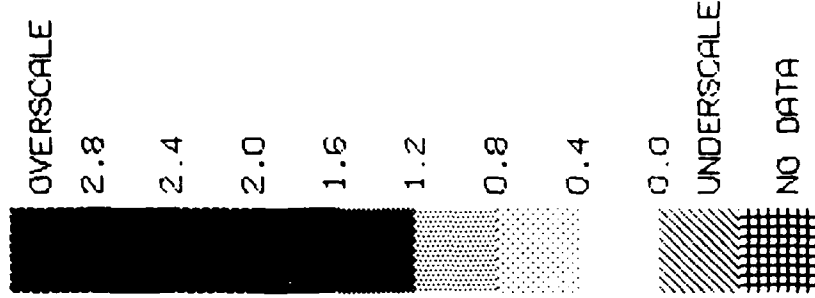
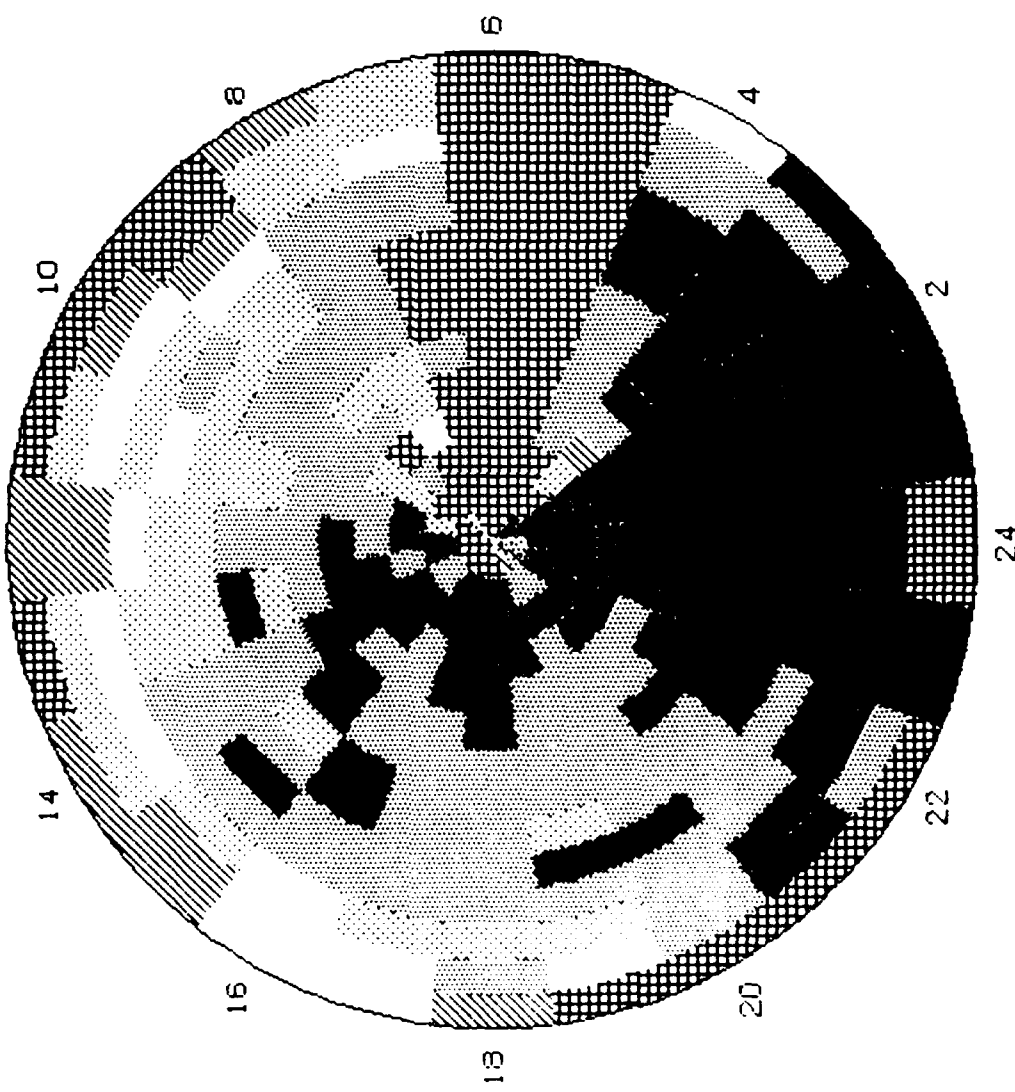
KP = 4-10 9 PLASMA DENSITY SPECTRAL SLOPE





KP = 4-10.9

PLASMA DENSITY SPECTRAL SLOPE



END

8-87

DTIC